Powder Technology 421 (2023) 118455

Contents lists available at ScienceDirect

Powder Technology

journal homepage: www.journals.elsevier.com/powder-technology

Compaction of highly deformable cohesive granular powders

Quan Ku [a], Jidong Zhao [a,b,*], Guilhem Mollon [c], Shiwei Zhao [a]

[a] Hong Kong University of Science and Technology, Clearwater Bay, Kowloon, Hong Kong
[b] HKUST Shenzhen-Hong Kong Collaborative Innovation Research Institute, Futian, Shenzhen, China
[c] Université de Lyon, INSA Lyon, CNRS, LaMCoS, UMR5259, 69621 Villeurbanne, France

HIGHLIGHTS

- We develop a multi-particle finite element method based on novel consideration of highly compressible, cohesive powder grains.
- The mechanical responses of cohesive powders are examined systematically under different loading conditions.
- The study offers new understandings toward the elastic, yielding, damage, and hysteresis responses of compacted granular powders.

GRAPHICAL ABSTRACT

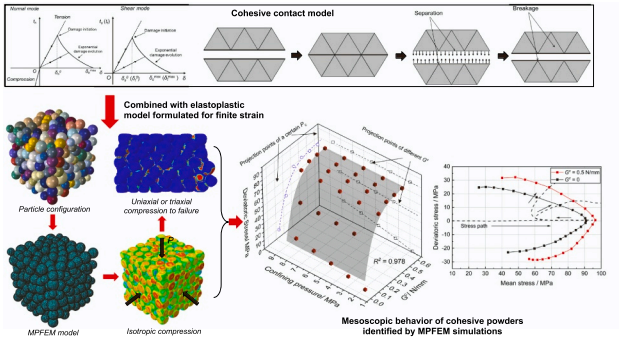

ARTICLE INFO

Keywords:
Granular powder
Compaction
Cohesion
MPFEM
Deformable particle

ABSTRACT

Compaction of granular powders underpins many engineering and industrial processes. The physics underlying the compaction process of highly deformable, cohesive granular powders remains poorly understood. A Multi-Particle Finite-Element Method (MPFEM) is presented to examine the mechanical responses of cohesive granular powders under compaction and decompaction. Each powder grain is assumed to be plastically deformable and is discretized by finite elements. Intergranular cohesion and its breakage are described by a cohesive inter-grain contact model. The proposed MPFEM is first validated and verified by powder grain contact problems. It is further employed for systematic simulations of the compaction of cohesive powder assembly under different loading paths, including unconfined compression, triaxial compression, and cycling loading. The simulation results are systematically analyzed and discussed pertaining to the elastic, yielding, damage, and hysteresis responses of the compacted powder assembly in relation with the constituent powder grains. Quantitative correlations are identified between the elastic recovery and Young's modulus of the compacted powder assembly with the relative density and the Young's modulus of individual powder grains. Maximum relative density under the compaction is found positively correlated with both unconfined and triaxial compression strengths of the assembly. Inter-particle bond strength is found to play an important role in shaping the yield surface and enhancing the strain hardening behavior of the powder assembly. While the unconfined compressive strength of the powder assembly shows an exponential increase with bond strength, the Young's modulus is found to increase to a saturated value with bond strength. The study provides an effective numerical approach to simulate the

* Corresponding author at: Hong Kong University of Science and Technology, Clearwater Bay, Kowloon, Hong Kong.
E-mail address: jzhao@ust.hk (J. Zhao).

https://doi.org/10.1016/j.powtec.2023.118455
Received 13 January 2023; Received in revised form 10 March 2023; Accepted 13 March 2023
Available online 16 March 2023

mechanical responses on dense compaction of cohesive, plastically deformable granular materials and helps shed lights into the understanding of powder compaction.

1. Introduction

Compaction of granular media such as powders is a crucial process relevant to pharmaceutics, metallurgy, and chemical and civil engineering. In pharmaceutical industry, for example, powders are typically filled into a die and compressed under a specific pressure to form a solid tablet. Multiple mechanisms come into play during such process, including particle rearrangement, interlocking and adhesion, elastic and plastic deformation, and possible particle breakage [18,63]. Among many design indices, porosity is a key parameter to assess the quality of powder compaction. It is desirable to achieve high-quality tableted products of relatively low porosity, but it remains a challenge [3] which is frequently related to complex mechanical responses of powders under compaction. The initial compaction stage of granular powders of lower densities is typically featured by particle rearrangements and dominant elastic responses, which is relatively well understood [64]. When the powders are compacted to a relatively higher density, however, individual powder grains may undergo significant plastic deformation, causing great increased mechanical particle interlocking and strengthened bonds due to increased contact areas [66]. How the mechanical behavior of compacted powders is related to the high plastic deformation of individual powders and changes of inter-particle processes such as bonding and debonding remains relatively less understood and has attracted considerable efforts by the research community.

Early studies on powder compaction have yielded some useful, simplified empirical solutions to establishing the relationship between the porosity and applied pressure during powder compaction in a die [32,39]. These solutions have been successfully applied to predicting the compaction of ceramic [62], metal [60], and pharmaceutical [91] powders. Despite their practical usefulness, these analytical equations offer little to understanding on both micro and macro scale physical and mechanical properties of powders related to their compaction [15]. Advances in experimental testing and observational tools, including X-ray computed tomography, greatly facilitate the measurements and analyses of all aspects of powder compaction [5,10,35]. Meanwhile, numerical simulations have been popularly used to examine the behavior of compacted powder. Among many, finite element method (FEM) and discrete element method (DEM) are two recent prevailing numerical methods. FEM typically employs phenomenological constitutive models, such as the Drucker-Prager Cap model and the Cam-Clay model, [16,77,85,89,93], to simulate the powder compaction process and predict the mechanical responses, including stress, strain, and relative density distribution. It is sometimes difficult to rigorously calibrate the parameters of these continuum-based models due to their phenomenological nature. DEM offers an effective means to investigate the powder behavior based on the micromechanical considerations of powder grains. Each powder particle is represented in DEM by a discrete element to allow various physical processes at grain scale, such as interparticle contacts, rolling and sliding, friction, cohesion, and adhesion, collectively and naturally emerge as macroscopic mechanical responses of compacted powders [11,22,46,56,57,71,75]. The past decade witnesses an increasing number of novel DEM studies on high density granular compaction [23,24,29,36,65] that lead to significantly improved understanding of the multiscale behavior of powder compaction. One major limitation, however, has been the general assumption of slightly deformable or totally rigid particles in DEM, which prevents realistic account for the possible development of high deformation in a powder grain and hinders the reproduction of significant plastic deformation of powders that is widely observed in experiments, especially at high density.

To model highly deformable particles, the Multi-Particle Finite Element Method (MPFEM, [21]) has stood out among various recent attempts to become a popular method used in different research areas, including granular physics [47], geophysics [43], and tribology [83]. MPFEM features a combination of FEM and DEM, where each grain is discretized into finite element meshes for resolved grain deformation, and the DEM is employed to handle the contacts between deformed grains. There are variant of MPFEM, such as non-smooth contact dynamics (NSCD, **[7,8,82]**), where unilateral contact conditions are considered for FEM nodes. MPFEM helps to bypasses the need for regularization of coefficients for the contact laws in traditional DEM [12], and offers relatively robust and stable solution to modelling of deformable powder grains. It has been increasingly used in recent studies of powder compaction, for both 2D [27,61,86] and 3D [20,26] conditions in conjunction with different powder materials [27,37], powder grain shapes [14], and initial packings [90]. These studies have led to improved understanding of the underlying mechanics and physics of the compaction process of powders. In particular, the yielding and plasticity of powder grains have been thoroughly investigated by Schmidt et al. [69,70]. Based on the energy criteria proposed by Schmidt et al. [68], Harthong et al. [28] and Abdelmoula et al. [2] further established the yield surfaces of compacted powder under complex loading histories and determined the direction of inelastic flow. Güner et al. [25] explored the effect of different contact friction models during closed-die compaction to examine the interaction between powder particles. Meshless FEM [48–51,53] has more recently been developed to account for large deformation of granular grains. In addition to DEM and FEM, some emerging numerical methods such as molecular dynamics [41,42,45,74] can also be employed for powder compaction simulation. Although molecular dynamics has so far only considered at the nanoscale, it can consider contact and plastic deformation of particles from a more fundamental level.

The complexity of powder compaction arises from the intertwined interplays among large inelastic deformation of powder grains, significant mechanical particle interlocking, evolving contact surface with grain deformation, changing interparticle cohesion developed at contacts, and complex loading paths including cyclic loading and unloading. Existing studies have not been able to adequately account for all these aspects to offer a systematic investigation of powder compaction toward a more understanding of the process. The objective of this paper is to critically address these issues based on a systematic numerical study on powder compaction. To this end, the MPFEM is extended to consider highly deformable powder grains that can develop significant plastic deformation and interparticle cohesion which may further undergo debonding when subjected to unloading or reverse shearing. Based on the numerical results, the behavior of compacted powders is comprehensively examined pertaining to their elasticity, plastic yielding, damage, and hysteresis, to shed lights into a theoretical basis for future study of the mechanics and physics of powder compaction.

2. Theoretical consideration of powder compaction

The multi-particle finite element method (MPFEM) is employed to model the powder compaction process in this study. As shown in Fig. 1 (a), each spherical powder in MPFEM is discretized by 4-noded linear tetrahedron finite elements. An elastoplastic model implemented in finite strain formulation is proposed to simulate each powder as a highly deformable solid grain. When two powder grains are in contact, cohesive bonds are assumed to develop at the contact area to form a solid bridge as shown in Figs. 1 (b) and (c). A rigorous cohesive contact model is further proposed to describe the formation and breakage of such a bond under changing loading conditions. The following presents the

various constitutive and computational considerations for simulation of powder compaction.

2.1. Elasto-plastic description of deformable powder grain

The following von Mises-type power-law plastic model in conjunction with an isotropic linear elastic relation is employed to describe the material response of each Gauss integration point of the elements for each powder grain [2,29]:

$$\sqrt{\frac{3}{2}S_{ij}S_{ij}} = \sigma_y + k\left(\sqrt{\frac{2}{3}\epsilon^p_{ij}\epsilon^p_{ij}}\right)^m \tag{1}$$

where σ_y is the yield stress, S_{ij} and ϵ^p_{ij} are the deviatoric stress tensor and deviatoric plastic strain tensor, respectively, and k and m are two hardening parameters. The Young's modulus E and the Poisson ratio ν are used to describe the isotropic linear elastic response. Without loss of generality, we choose a specific granular powder, Microcrystalline Cellulose (MCC) 102 powders, as a demonstrative example for the study. The MCC powders have widely served as a useful additive in pharmaceutical and many other industries [17]. For MCC powders, we adopt the following model parameters following Yohannes et al. [88]: $\sigma_y = 25$ MPa, $k = 125$ MPa, $m = 0.3$, $E = 5$ GPa, and $\nu = 0.3$. Since plastic deformation is dominant over elastic strain for the MCC powders, this study adopts the assumption of linear elastic relation for the elastic behavior.

The constitutive relation in Eq. (1) has been expressed in terms of Cauchy stress and true strain to facilitate easy comprehension. FEM implementation of the model has been formulated within finite strain theory to allow the simulations to capture the high deformability of granular powder grains. Specifically, the Jaumann objective rate of Cauchy stress is adopted to account for large rotation and large displacement a typical powder particle may undergo during compaction. The logarithmic strain based on the deformation rate and its time integral is employed as a strain measure. An explicit time integration scheme is used to calculate the displacement increment in a typical incremental linearization of nonlinear problem. Detailed formulations these quantities and the explicit integration scheme follow the standard formulations [1] which will not be repeated here to avoid excess defocusing of the present study.

2.2. Cohesive contact model between powder grains

We consider a class of granular powders which may gradually establish interparticle solid bridge at mechanical contacts between powder grains when subjected to external loadings. Upon change of loading conditions, such a solid bridge may also undergo breakage (or debonding) whose behavior is assumed to be described by the linear fracture mechanics [22]. Long-range attractive forces at molecular scale, such as van der Waals and hydrogen bonding interactions, are not considered here, since the dissociation energy of the solid bridge is about one or two orders of magnitude greater than that of these attractive forces [55]. Specifically, the following cohesive contact model is proposed to describe the formation and debonding process of the solid bridge between contacted powders. A schematic illustration of the multi-staged developments is shown in Fig. 2. Each powder grain is assumed to be cohesionless before a contact is developed with its neighboring grain (Fig. 2a). Once the surfaces of two grains come into contact, the surfaces are assumed to 'stick' to each other to form a cohesive solid bridge (Fig. 2b) with prescribed strength to be described below. The cohesive force of the solid bridge does not come into play until the two contacted surfaces start to open or slide (Fig. 2c) under certain conditions, before a complete breakage stage is reached when the contacted grains are totally separated (Fig. 2 (d)). The gradual opening or sliding process of two contacted surfaces is described by the degradation of the cohesive force following a traction-separation law illustrated in Fig. 3. Note that such traction-separation damage laws have been widely used for description of geomaterials, in conjunction with the zero-thickness cohesive elements in FDEM to simulate breakage behavior of rocks and sands [52,84,92].

Fig. 3 shows the elastic-exponential damage law employed in the study to describe the traction-separation behavior of cohesive contact [59] for both normal and shear directions between powder particles. This study adopts the penalty contact enforcement to allow a negative contact distance (penetration) as shown in Fig. 3(a). The default penalty stiffness is based on a representative stiffness of the underlying elements to minimize the influence of the choice of time increment and ensure the allowed penetration is not significant [1].

Specifically, the following linear elastic relation is used to model the pre-peak elastic response:

$$\mathbf{t} = \mathbf{D}\boldsymbol{\delta} = \begin{Bmatrix} t_n \\ t_s \\ t_t \end{Bmatrix} = \begin{bmatrix} E_{nn} & E_{ns} & E_{nt} \\ E_{ns} & E_{ss} & E_{st} \\ E_{nt} & E_{st} & E_{tt} \end{bmatrix} \begin{Bmatrix} \delta_n \\ \delta_s \\ \delta_t \end{Bmatrix}, \tag{2}$$

where $\mathbf{t}$ is the traction vector, $\mathbf{D}$ the elastic stiffness matrix, and $\boldsymbol{\delta}$ the separation displacements between the two surfaces. The subscripts n, s, and t denote the normal and two tangential directions, respectively. The initiation of damage of the cohesive bond is assumed to be governed by the following quadratic nominal failure criterion:

$$\left(\frac{\langle t_n \rangle}{t^m_n}\right)^2 + \left(\frac{t_s}{t^m_t}\right)^2 + \left(\frac{t_t}{t^m_t}\right)^2 = 1, \tag{3}$$

where $\langle \bullet \rangle$ is the Macaulay bracket, t^m_n, t^m_t and t^m_s are the threshold stress

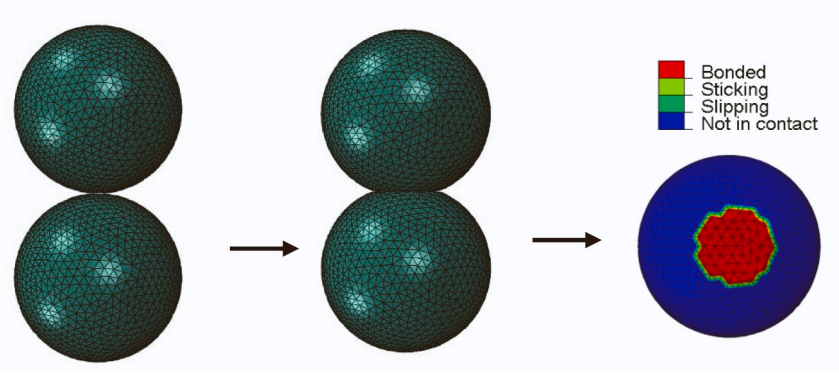

Fig. 1. Simulation of two deformable powder grains developing cohesive bond at contact by multi-sphere finite element method (MPFEM): (a) before contact, (b) under contact, and (c) formation of cohesive bonds (view from the contact area).

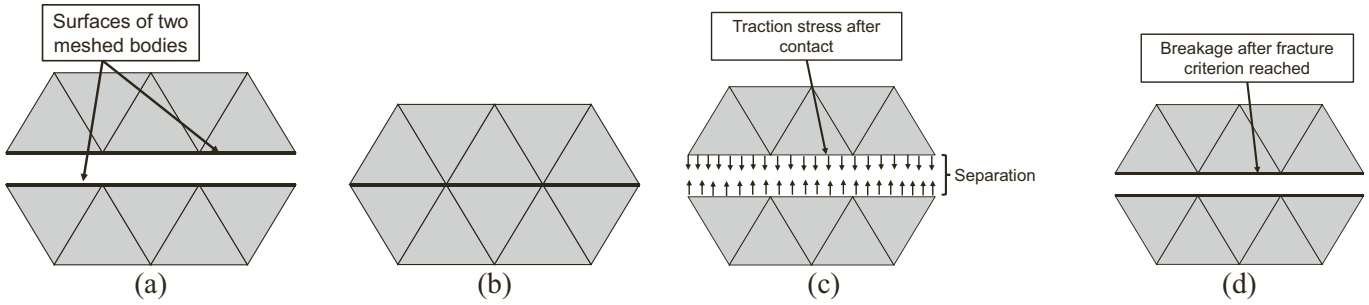

Fig. 2. Illustration of the formation and breakage of a cohesive solid bridge between contacted surfaces: (a) Prior to the formation when two surfaces are not in contact; (b) During the formation when the clearance between two surfaces is reduced to zero for further interpenetration of the two surfaces; (c) During the contact separation when the contact pressure gradually drops to zero and cohesive traction forces begin to develop between the two separating surfaces which tend to prevent the separation; (d) After total contact separation when the cohesive force drops to zero.

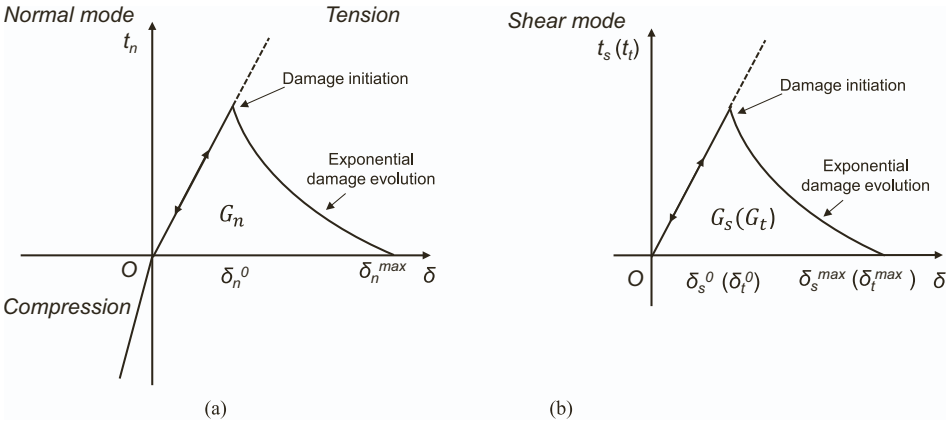

Fig. 3. Traction-separation laws to describe the breakage of solid bridge for: (a) normal and (b) shear modes.

along the three directions, respectively. Once the above criterion is met, the damage starts to evolute, and the cohesive stress of the cohesive bond is assumed to degrade following an exponential law (see Fig. 3). The post-peak stiffness degradation of the solid bridge is described by the following isotropic damage evolution law:

$$\begin{cases} t_n = (1-D)\bar{t}_n, \bar{t}_n \geq 0 \\ t_s = (1-D)\bar{t}_s \\ t_t = (1-D)\bar{t}_t \end{cases}, \tag{4}$$

where $\bar{t}_n$, $\bar{t}_s$, and $\bar{t}_t$ are the contact stresses calculated from the elastic stiffness matrix at the current separation without considering damage, and D is an irreversible damage variable, calculated according to [1]:

$$D = \int_{\delta_m^0}^{\delta_m^{max}} \frac{T_{eff}}{G^c - G^0} d\delta, \tag{5}$$

where δ_m^0 denotes the effective separations at the initiation of damage, δ_m^{max} is the maximum effective separation attained during the loading history, and δ_m is the effective separation defined by [6]:

$$\delta_m = \sqrt{\langle \delta_n \rangle^2 + \delta_s^2 + \delta_t^2}. \tag{6}$$

It is noting that D is irreversible since D is related to δ_m^{max} rather than δ_m. The effective traction T_{eff} in Eq. (5) is defined by

$$T_{eff} = \sqrt{\langle t_n \rangle^2 + t_s^2 + t_t^2}. \tag{7}$$

G^c and G^0 in Eq. (5) represent respectively the specific fracture energy and its reference elastic energy at damage initiation. Serving as a key factor in characterizing the fracture behavior, the specific fracture energy G^c is defined as the energy required per unit area to open the crack surface. This study employs the mode-independent damage evolution dependent on G^c only where the reference and current fracture energy is assumed to be expressed in an additive form as $G_n + G_s + G_t$, where G_n, G_s, and G_t are the fracture energies required by the traction and its conjugate relative displacement in the normal and the two shear directions, respectively. The fracture energy is employed to characterize the strength of the bonds between the contacted grains in this study.

Granular powders are commonly frictional. However, a coupled consideration of cohesion and friction may greatly complicate the description of tangential contact for highly deformation particles. Further consideration of damage mechanism of the cohesive bond in large deformation regime for each particle may make it challenging to formulate theoretically and implement numerically. Hence friction is not considered in this study for convenience. Indeed, Venzal et al. [81] argued that the involvement of friction resistance, such as in form of a subtracted term from the mechanical response along the shear plane, may lead to underestimation of the cohesive energy in the tangential direction. Under axisymmetric loading such as compaction, it is a widely accepted consensus that the tangential contact plays a less important role than its normal counterpart [9,58]. For simplicity, the focus of this study is placed upon isolating the influences of cohesion while neglecting the effect of friction. The coupling effect of friction and cohesion on powder compaction will be left in a future study.

3. Model validation and verification

The elastoplastic powder grain model and cohesive contact model for the solid bridge presented in Section 2 have been implemented in Abaqus [1]. The implemented multi-sphere finite element method (MPFEM) is first validated before it is used for powder compaction

simulation. Table 1 presents the model parameters calibrated for the following study. Both the normal and tangential contact stiffnesses adopt a value ten times of the element stiffness to render balanced accuracy and numerical stability [1]. Note that Tatone and Grasselli [79] have suggested values of infinity for them in their FDEM study. The tensile strength of MCC adopted is based on the experimental study of Mashadi and Newton [44], and the fracture energy according to Yohannes et al. [88]. A shear strength 0.5–0.7 times the tensile strength is generally considered reasonable for the cohesive bonds.

3.1. Validation of the MPFEM implementation of cohesive contact model

The implemented MPFEM is validated by predictions of normal contact between two spheres, for both the small elastic strain regime and plastic strain regime. Since most analytical solutions are available only for Hertzian elastic contact in small strain regime, the elastic-cohesive contact of the proposed numerical approach is first validated. Specifically, the MPFEM prediction is benchmarked against the classical elastic adhesion theory proposed by Johnson, Kendall, and Roberts ([38], hereafter denoted as JKR theory). The JKR theory has been shown to be able to capture adhesive contact behavior of an elastic spherical particle at relatively large deformation [78]. As shown in Fig. 4 (a), two identical hemispheres with a radius of $R = 0.1$ mm discretized by a total of 117,070 tetrahedral finite elements (for each) with refined mesh at the contact area are brought into compressive contact before a gradual release to allow a loading and unloading process. The adopted elastic parameters are shown in Table 1. The fracture energy adopted in our cohesive contact model is considered equivalent to the surface energy in the JKR theory. Note that the classical JKR theory does not consider the tangential adhesion. Therefore, our numerical model has been set up to produce cohesive normal contact only for validation.

Both loading and unloading curves with three different cases of fracture energy are illustrated in Fig. 4(b). The overlap h is defined as $h = R_1 + R_2 - \|\boldsymbol{x}_1 - \boldsymbol{x}_2\|$, where R and $\boldsymbol{x}$ are the radius and the location of the center of the two contacting spheres. The normalized contact force is defined as $F/(ER^2)$ where F and E are the contact force and the Young's modulus of each sphere, respectively. The loading process agrees with the Hertzian contact model reasonably well. Since cohesion does not play a role in the purely normal compression loading stage, predictions of the loading stage for all three fracture energy cases collapse identical values. The effect of fracture energy only manifests itself during the unloading stage (the bottom three curves/date points in green, red, and blue). The cohesion formed by normal contact between grains starts to play an apparent role in resisting the separation of the two contacted surfaces by generating tensile force. Evidently, the MPFEM simulations are in good agreement with the JKR solution.

A similar model setup as shown in Fig. 4(a) is chosen for the second validation example where relatively large plastic deformation is allowed to develop between the contact area during a typical loading-unloading cycle. The comparison is made against the analytical model proposed by Gonzalez [22]. Gonzalez [22] adopted the following simple model, by replacing the plastic strain in Eq. (1) with true strain, to describe the plastic behavior of powder grains:

Table 1
Properties of powder grains and cohesive contact model.

	Parameter	Value
Elasto-plastic model	Elastic modulus, E (GPa)	5
	Poisson's ratio, ν	0.3
	Yield stress, σ_y (MPa)	25
	Strength coefficient, k (MPa)	125
	Hardening exponent, m	0.3
Cohesive contact model	Tensile strength, t_n^m (MPa)	25
	First shear strength, t_s^m (MPa)	18
	Second shear strength, t_t^m (MPa)	18
	Fracture energy, G^c (N/mm)	0.5

$$\sqrt{\frac{3}{2}S_{ij}S_{ij}} = n\left(\sqrt{\frac{2}{3}E_{ij}E_{ij}}\right)^p \tag{8}$$

where E_{ij} is the true strain including both plastic and elastic strains. n and p are two hardening parameters similar to Eq. (1) which are calibrated as $n = 160$ MPa and $p = 0.4$ for the following comparison [29]. The fracture energy used in the cohesive contact is $G^c = 0.01$ N/mm, which corresponds to an equivalent fracture toughness $K_{Ic} = 0.23$ MPa $m^{1/2}$ according to: $K_{Ic} = \sqrt{2G^c\overline{E}}$, where $\overline{E}$ is the effective elastic stiffness for two contacting spheres:$\overline{E} = \left(\frac{1-\nu_1^2}{E_1} + \frac{1-\nu_2^2}{E_2}\right)^{-1}$.

Fig. 5 presents a comparison of our model simulations of the normal compression and decompression responses of two identical MCC CP102 powder grains with predictions by Eq. (8) at three loading cases. Different colors are adopted in the plot to represent three different loading distances. It is evident from Fig. 5(a) that our proposed model predicts rather consistent loading and unloading responses of the elasto-plastic cohesive contact behavior between the two powder spheres with the analytical solution in Eq. (8), even when relatively large plastic deformation is developed at the contact. Fig. 5(c) further presents the damage distribution of the cohesion along the contact area at the end of the unloading process.

3.2. Model setup for powder compaction and mesh sensitivity study

We consider a packing of 329 spherical particles as shown in Fig. 6 to study the compaction process of deformable, cohesive powders for the rest of this paper. The particle size distribution of these spheres follows the typical sizes of Microcrystalline Cellulose (MCC) CP102 powders as measured by Domike [17]. Fig. 6(b) shows the cumulative particle size distribution used in the following study. These spheres are randomly packed in a cubic box with a side length of 0.95 mm confined by smooth rigid walls. The initial relative density of the generated packing D_r (i.e., the ratio of the volume occupied by all spheres to the total volume of the entire assembly) is 0.552. There are no initial contacts between the particles, ensuring that the particles do not penetrate each other after the finite element mesh is generated for each sphere. Fig. 6(a) shows the original assembly of spherical grains after such generation.

Discretization error is notably important for FEM and many other numerical discretization schemes. The issue is especially critical for MPFEM simulation of powders since the mesh resolution may further affect the contact behavior between powder grains. To this end, four different mesh sizes are examined on the sensitivity of simulation results to mesh size. Fig. 7 shows the FEM packings with different mesh sizes (0.03 mm, 0.025 mm, 0.015 mm, and 0.0075 mm) which contain 188,760, 342,919, 1,599,106, and 12,015,373 tetrahedral elements, respectively. Each packing is then isotropically compressed (or isotropic consolidation) to a relative density $D_r = 0.92$. The loading the sufficiently slow to ensure quasi-static conditions. Fig. 8 shows the predicted von Mises stress distribution at the central cross-section of the packing for the four mesh cases. Evidently, higher stress resolution is obtained with finer mesh size. The stress concentration at interparticle contacts can be better captured by smaller mesh size than coarse mesh. Fig. 9 further shows the consistency of the predicted relationship between relative density and overall mean stress for the four mesh cases. It is apparent that the refinement of mesh helps to gain consistent prediction where the curves of 0.0075 mm and 0.015 mm cases are sufficiently close to render consistency. All subsequent simulations have been using the mesh size of 0.015 mm, based on a balanced consideration of computation efficiency and accuracy. The mass scaling method has also been used in this study to speed up the computation.

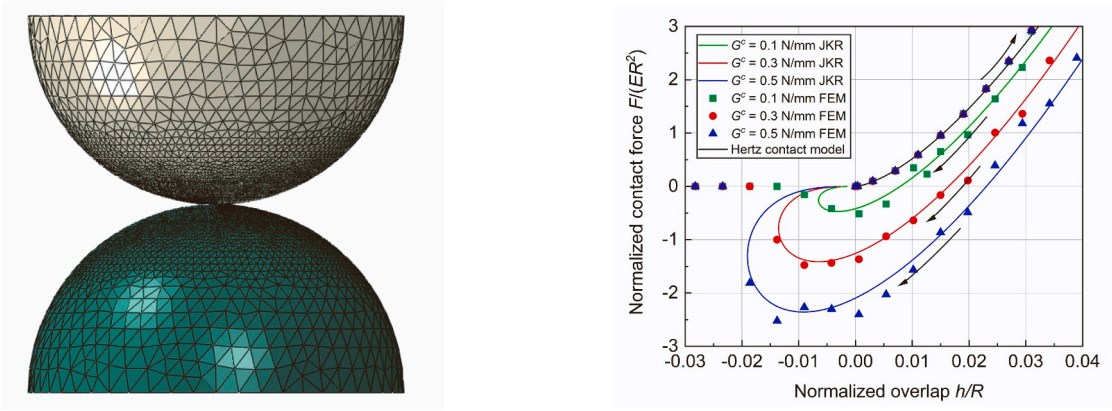

Fig. 4. Contact validation for spheres, (a) two meshed hemispheres, (b) loading and unloading curves with different fracture energy.

4. Simulation on compaction of cohesive, highly deformable powders

Systematic numerical simulations will be performed to explore the following aspects of the compaction of cohesive powders, elastic recovery, mechanical response, and strength of compacted powders under uniaxial and triaxial compressions and cyclic loading conditions. Further discussion will be devoted to the micromechanical attributes of the various macroscopic observations.

4.1. Elastic recovery

Key to powder compaction is the evaluation of elastic recovery which is considered to directly account for such phenomena as capping and lamination in pharmaceutical tablet production [80]. Indeed, elastic recovery is the negative elastic volumetric strain that occurs during the unloading process of packing. The elastic recovery R_E can be determined according to the maximum relative density (D_r^{max}) during the loading stage and the minimum relative density (D_r^{min}) at the end of unloading as follows:

$$R_E = \frac{D_r^{max} - D_r^{min}}{D_r^{max}} \tag{9}$$

where D_r^{max} is the desired relative density in design, and hence it is practically preferred to have the elastic recovery as small as possible. To examine the dominant factors of elastic recovery, simulations are performed for powder grains subjected to isotropic compression first to a specific relative density before isotropic unloading to zero confinement. Van der Voort Maarschalk et al. [80] argued that the relief of locked in elastic energy may cause the powder material with a high bonding capacity to laminate or cap. Therefore, the locked in elastic energy release and bond strength may be important factors affecting the behavior of elastic recovery or capping of compacted powders and will be investigated here. The following factors are chosen to examine their correlations with the elastic recovery: the maximum relative density D_r^{max} and the Young's modulus of powder grain E. How these parameters affect the elastic strain energy and the damage dissipation of the assembly is systematically investigated.

To quantify how the designed maximum relative density affects the elastic recovery, we fix all models parameter in Table 1. Fig. 10(a) shows a linear correlation between the elastic recovery and the maximum relative density identified from our study, which is consistent, both in the overall trend and order of magnitude, with the experimental observations reported by Keizer and Kleinebudde [40]. Fig. 10(a) shows an interesting bi-linear relationship between the maximum relative density and the elastic recovery, with an intersection at a relative density of around 0.859. The slope of the fitted line for the higher relative density portion is greater than the lower part. Indeed, the extent of deformation a powder grain may undergo is found positively correlated with the elastic energy it can store and the total recoverable volume [31]. As the maximum relative density becomes higher, the grains in the packing deform more severely with higher locked in elastic energy, resulting in potentially greater elastic recovery. The increase of slope in the bi-linear relationship at higher maximum relative density >0.86 may be closely related to the relative dominance of stored elastic energy and the effect of cohesion. If a granular powder experiences a larger maximum relative density before unloading, the release of the stored elastic strain energy may overpower the restriction of developed cohesion and results in large elastic recovery and hence stiffer slope of the correlation.

To investigate the effect of elastic strain energy, we further vary the Young's modulus of the powder grain from 3000 MPa to 8000 MPa and compact the powders toward a designed $D_r^{max} = 0.92$. Except the Young's modulus, other mechanical parameters are kept consistent with Table 1. Within the considered range, a striking linear correlation is found between the elastic recovery and the Young's modulus of the powder grain in a double logarithmic plot as shown in Fig. 10(b). Fig. 11(a) further presents how the elastic strain energy of the ensemble evolves during the loading and unloading stages of the isotropic compression with different Young's moduli specified for the powder grain. The elastic strain energy (E_{es}), elastic strain energy release (E_{esr}), and damage dissipation energy (E_{dp}) are normalized by the Young's modulus of the grains (E) and the mean radius of the particles ($\overline{R}$) in this section. At the end of unloading, the elastic strain energy approaches a steady non-zero value, commonly termed as locked in elastic energy, when the elastic recovery is stabilized. Interestingly, the locked-in elastic energy of the system tends to be close after normalizing by the Young's modulus of the grains. Comparing to Fig. 11(c) for the elastic strain energy of the assemble without normalization, the elastic energy has no significant difference between samples with different Young's modulus during the loading stage. It can be reasonably inferred that the total elastic strain of the system during the loading stage is related to the elastic properties of the grains themselves, and the total elastic strain may be inversely proportional to the elastic modulus of the grains. After unloading and during the elastic recovery stage, the residual elastic strain of an assembly tends to be similar irrespective of the elastic properties of the grains. This indicates that the residual elastic strain of the assembly may only be related to the deformation and contact configuration of the particles. The above observation is found for a loading-unloading process dominated by compression without significance shear deformation (since friction is not considered). Its validity needs further to be verified in the frictional particle case.

Note that the elastic recovery may also involve substantial debonding processes between contacted powders during the compression

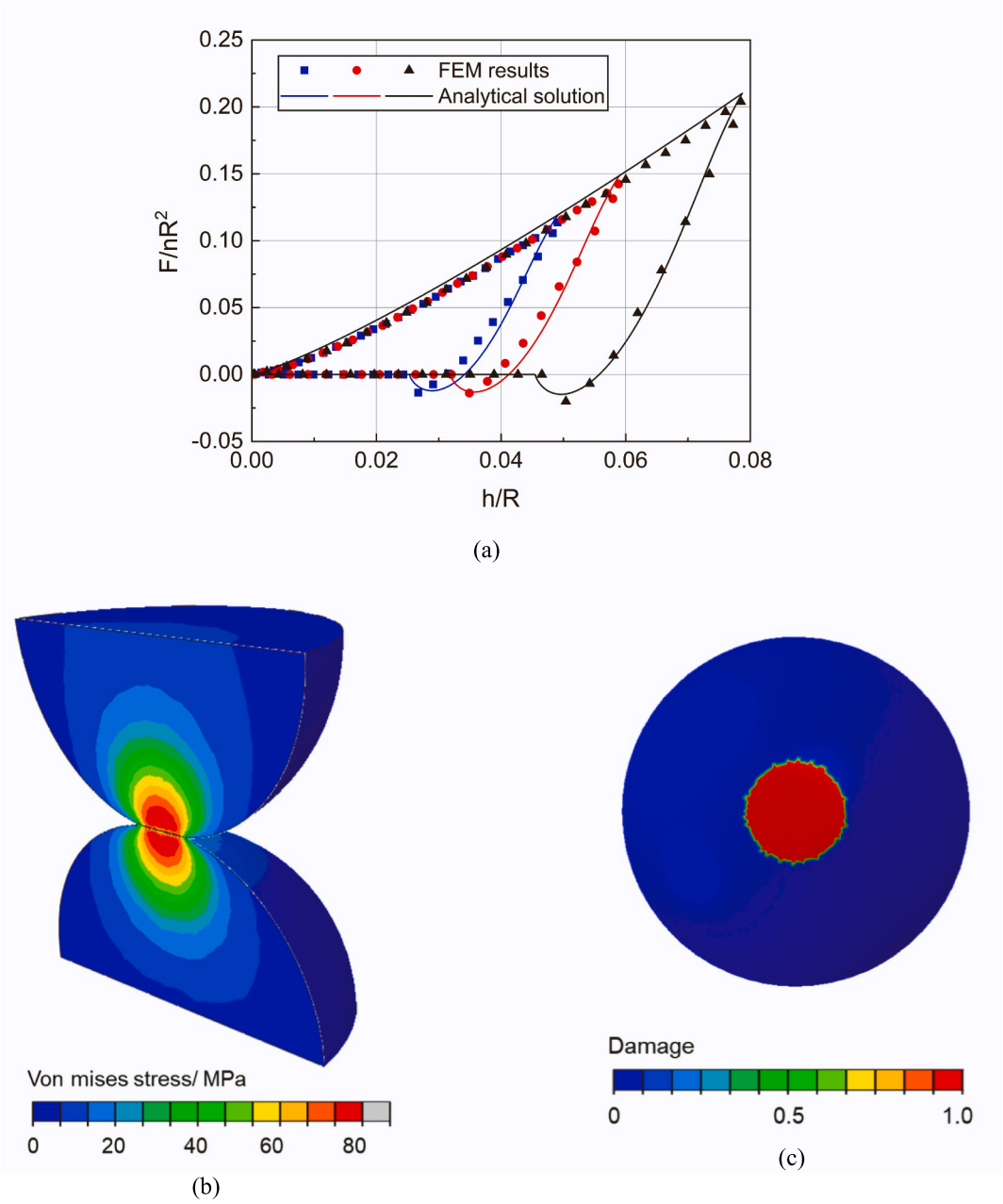

Fig. 5. (a) Validation of MPFEM prediction of the normal loading-unloading against analytical solution by Gonzalez [22] at three large strain level. (b) von Mises stress distribution at the contact area when h/R = 0.04(c) Damage distribution of the cohesion during the unloading stage (View from the contact area. Maximum h/R = 0.08).

process, which can be measured by the dissipation energy through damage. Note that the total dissipation energy through damage is the sum of fracture energy of the system.

Fig. 11(b) shows the change of the release of elastic strain energy and the total damage dissipated energy at the end of unloading for cases with different Young's moduli. The total damage energy dissipation is considered in this study to characterize the degree of damage to the cohesion. Evidently, the elastic recovery is featured by both elastic strain energy release and plastic dissipation, and the elastic strain release and damage dissipation are closely correlated with elastic recovery. Grains with higher Young's modulus lead to lower elastic recovery for the packing, and reduced elastic strain release and less damage dissipation for the system. The elastic strain release dominates over the damage dissipation during the process.

4.2. Young's modulus and uniaxial strength

It is instructive to further examine the unconfined compressive behavior of the powder assembly after elastic recovery. Indeed, the elastic modulus of compacted powders is commonly quantified under such condition [4]. A three-stage simulation for the case is designed: (1) the assembly is isotropically compressed to a specific D_r^{max}; (2) the sample is isotropically unloaded to a small confinement state to ensure the stability of the packing at the beginning of the third phase; and (3) only top and bottom plates apply reloading of compression while the lateral plates are keeping unloading and stay away from the sample to render unconfined compression of the assembly. The parameters used in determining the Young's modulus adopt the same as shown in Table 1.

It is interesting to examine the Young's modulus E_p during the elastic reloading of stage (3) as shown in Fig. 12(a). Note that the reloading line

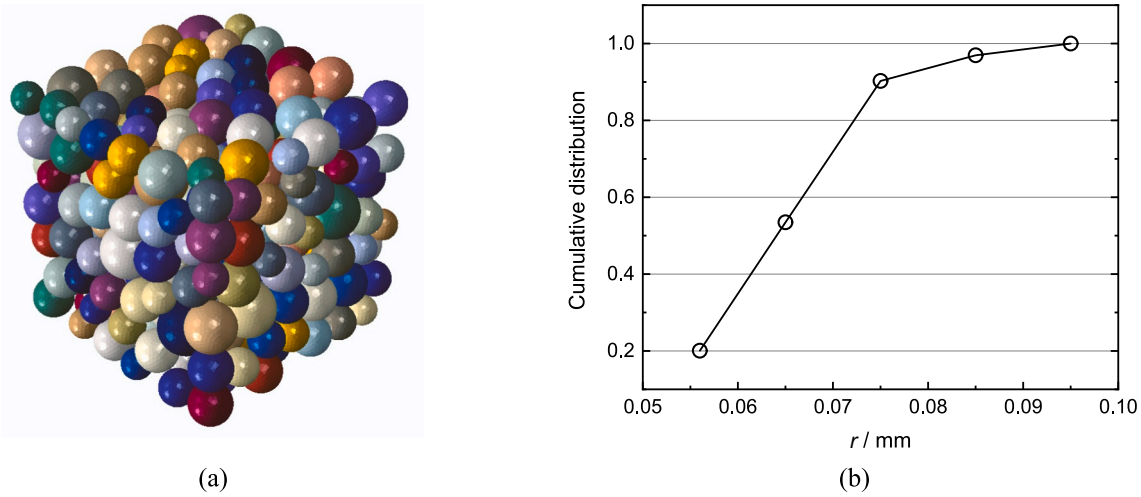

Fig. 6. The initial packing of spherical grains (a) and particle size distribution (b) generated for compaction of (MCC) CP102 powders.

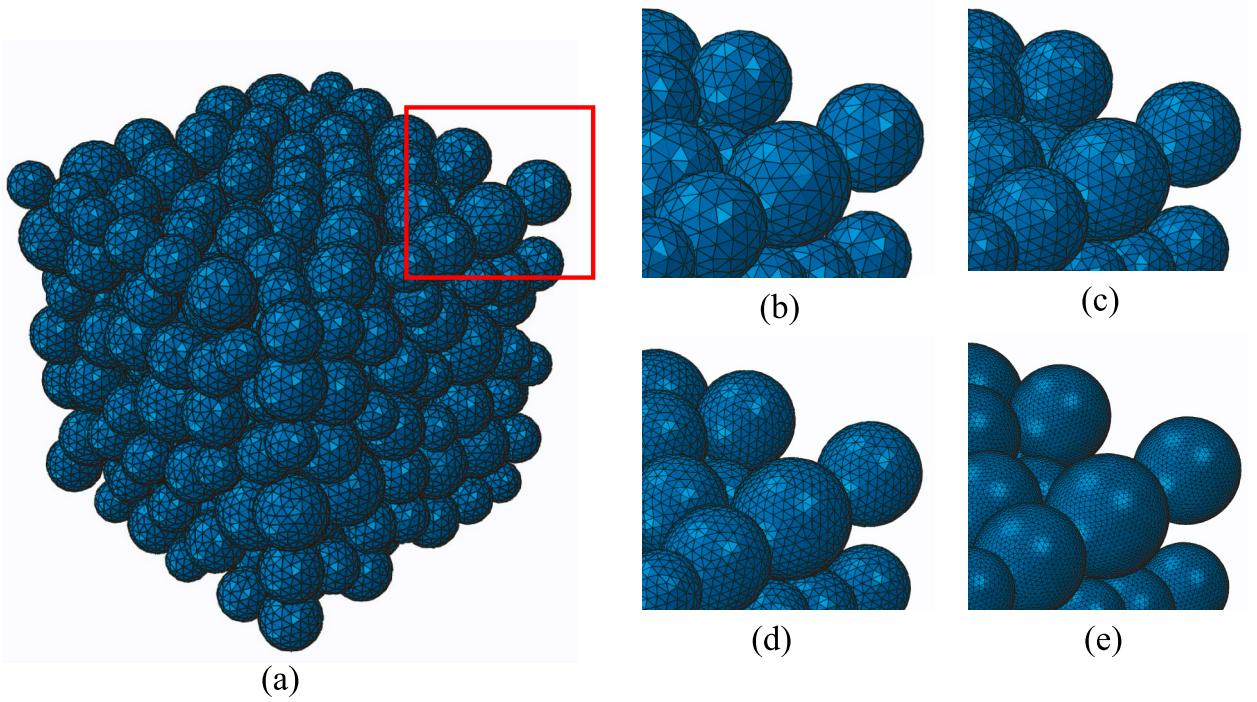

Fig. 7. MPFEM models with different mesh sizes for simulation of powder compaction. (a) Entire FEM packing of a mesh size at 0.03 mm and (b-e) locally zoomed meshes with a mesh size of 0.03 mm, 0.025 mm, 0.015 mm, and 0.0075 mm, respectively.

in Fig. 12(a) from the beginning of reloading before the yield or damage stage (e.g., circled in Fig. 12a) is selected in this study to determine the Young's modulus of the packing. The normalized Young's modulus, expressed by a normalized form by the Young's modulus of individual powder grain as E_p/E, is found to be positively correlated with the maximum relative density D_r^{max}. Understandably, denser compression (e.g., higher D_r^{max}) leads to larger contact areas between powders and stronger cohesion which further results in a higher Young's modulus for the powder assembly. An exponential correlation between the two is identified and shown in Fig. 12(b), which is consistent with the experimental observation by Sun et al. [76] on MCC powder. Spriggs [73] proposed the following empirical relationship between porosity and E_p/E based on experiments on polycrystalline refractory materials:

$$ln\frac{E_p}{E} = -aP \tag{10}$$

where a is a constant and P is the porosity of the powder assembly. Eq. (10) represents a curve passing through the point $E_p/E = 1$ and $P = 0$ ($D_r^{max} = 1$), irrespective of the elastic property of the powders [33]. According to Eq. (10), once the homogeneous grains are fully compacted without porosity (i.e., $P = 0$), the Young's modulus of the packing recovers the Young's modulus of the constituent grains. Mollon [48] found a similar pattern in the simulation of the shear behavior of deformable particles where the shear modulus of the dense packing with high relative density was found slightly lower than that of the grains. However similar it may show between our results with Eq. (10), our results in Fig. 12(b) does not precisely pass through the point $E_p/E = 1$ and $P = 0$. This deviation may be attributable to the debonding during the loading process, which will be discussed in a later section.

It is interesting to further examine the unconfined strength or uniaxial strength of the compacted powders. Our study shows that the

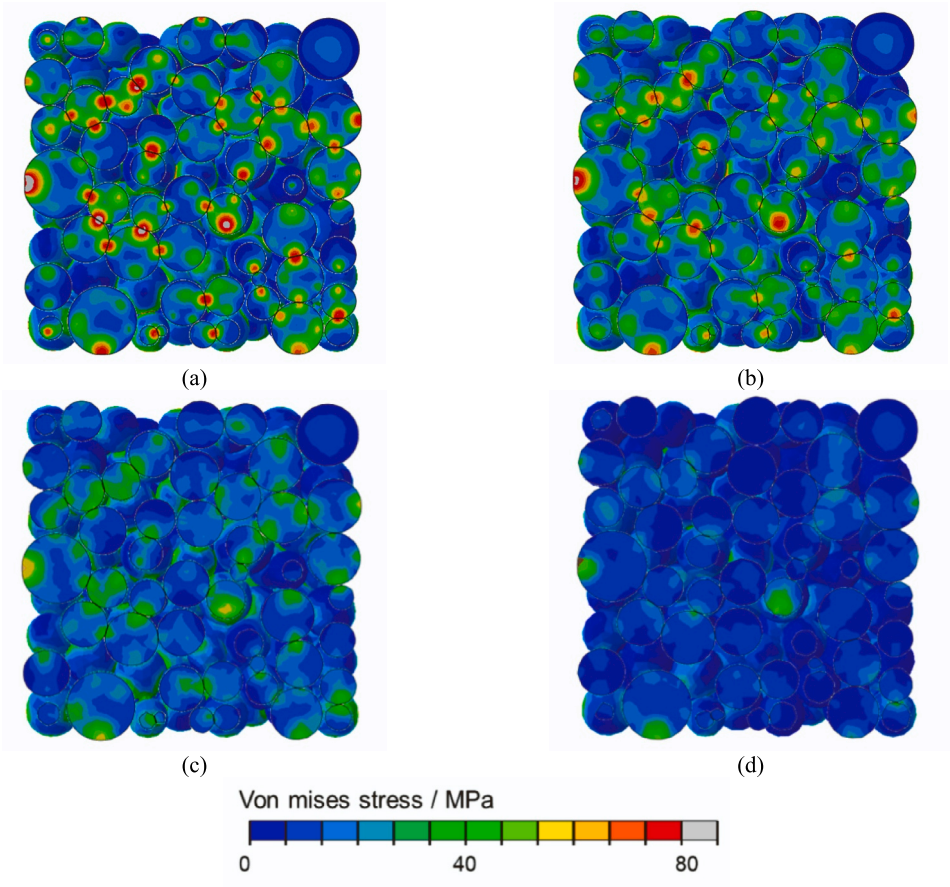

Fig. 8. Predicted Von Mises stress distribution for mesh size of (a) 0.0075 mm, (b) 0.015 mm, (c) 0.025 mm, and (d) 0.03 mm.

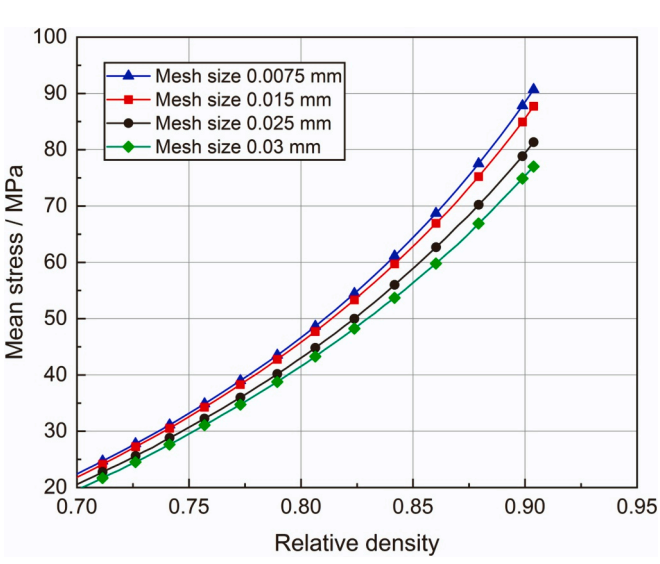

Fig. 9. Consistency study of the load-density at different mesh sizes.

packing does not show significant damage when the relative density and the fracture energy of the cohesion are high. Indeed, the propagation of cracks in a plastic material is significantly more difficult because plastic flow at the tip of a crack dissipates energy and retards crack propagation [19]. Therefore, in studying the uniaxial compression behavior, we have chosen a maximum relative density between 0.62 and 0.77 and set the fracture energy G^c of 0.3 N/mm. The uniaxial strength is defined as the vertical stress at the failure (coinciding with the onset of damage shown in Fig. 15). The uniaxial strength of an isotropically compacted powder assembly is found to increase exponentially with the maximum relative density D_r^{max}, as shown in Fig. 13(a). The relation between relative density and the uniaxial strength fit remarkably well with the Ryshkewitch-Duckworth equation ($R^2 = 0.996$). The empirical Ryshkewitch-Duckworth model [67] has been used by Smorodinov et al. [72] to describe the uniaxial compressive strength of rocks and by Hattiangadi and Bandyopadhyay [30] for ceramics:

$$\sigma = \sigma_0 exp(-BP) \tag{11}$$

where σ_0 is the strength of a non-porous sample, P is the sample porosity, and B is an empirical constant. Another seminal theoretical relationship between porosity and strength was proposed by Rumpf [66]:

$$\sigma = \frac{1-\varepsilon}{\varepsilon}\frac{F}{d^2} \tag{12}$$

where F is the mean tensile strength per unit cross-sectional area, d is the diameter of the primary particles and ε is the porosity. The Rumpf equation is concerned with tensile strength rather than compressive strength. Since the initiation of fracture needs to exceed the tensile strength in at least one direction, it is believed that the tensile strength has a strong correlation with the compressive strength (e.g., the ratio between tensile strength and compressive strength is constant. [34]). However, it is observed in Fig. 13(a) that the simulation results show a deviation from the fitting equation proposed by Rumpf [66], which may be attributable to the fact that the correlation of the compressive strength with tensile strength may be affected by other factors, such as amount of plastic yielding at the point of load application [13]. Therefore, it is advisable to use the Rumpf equation with caution to estimate the compressive strength of powders.

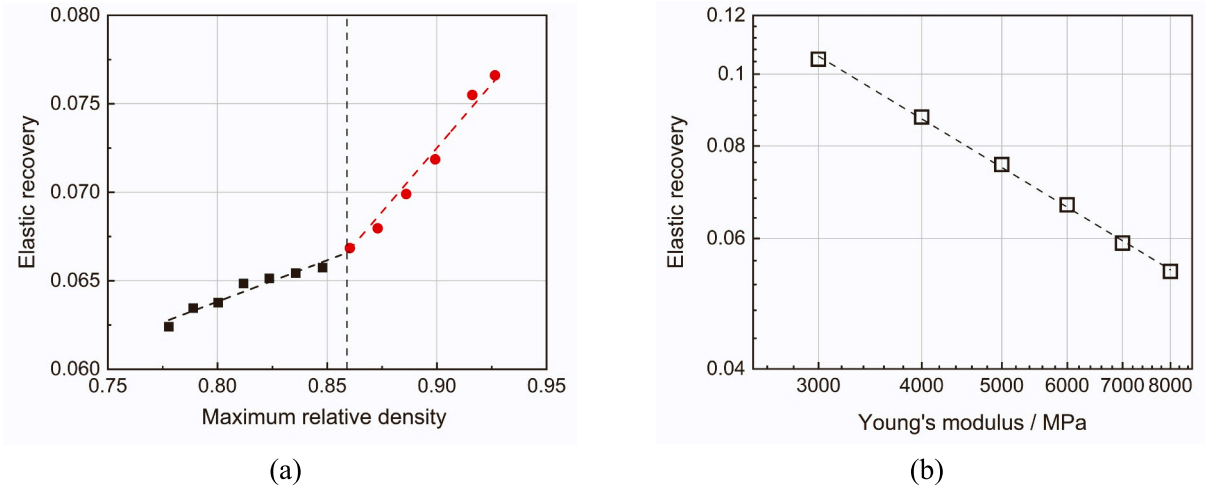

Fig. 10. Correlation between the elastic recovery and the maximum relative density (a) and the Young's modulus of powder grain (b).

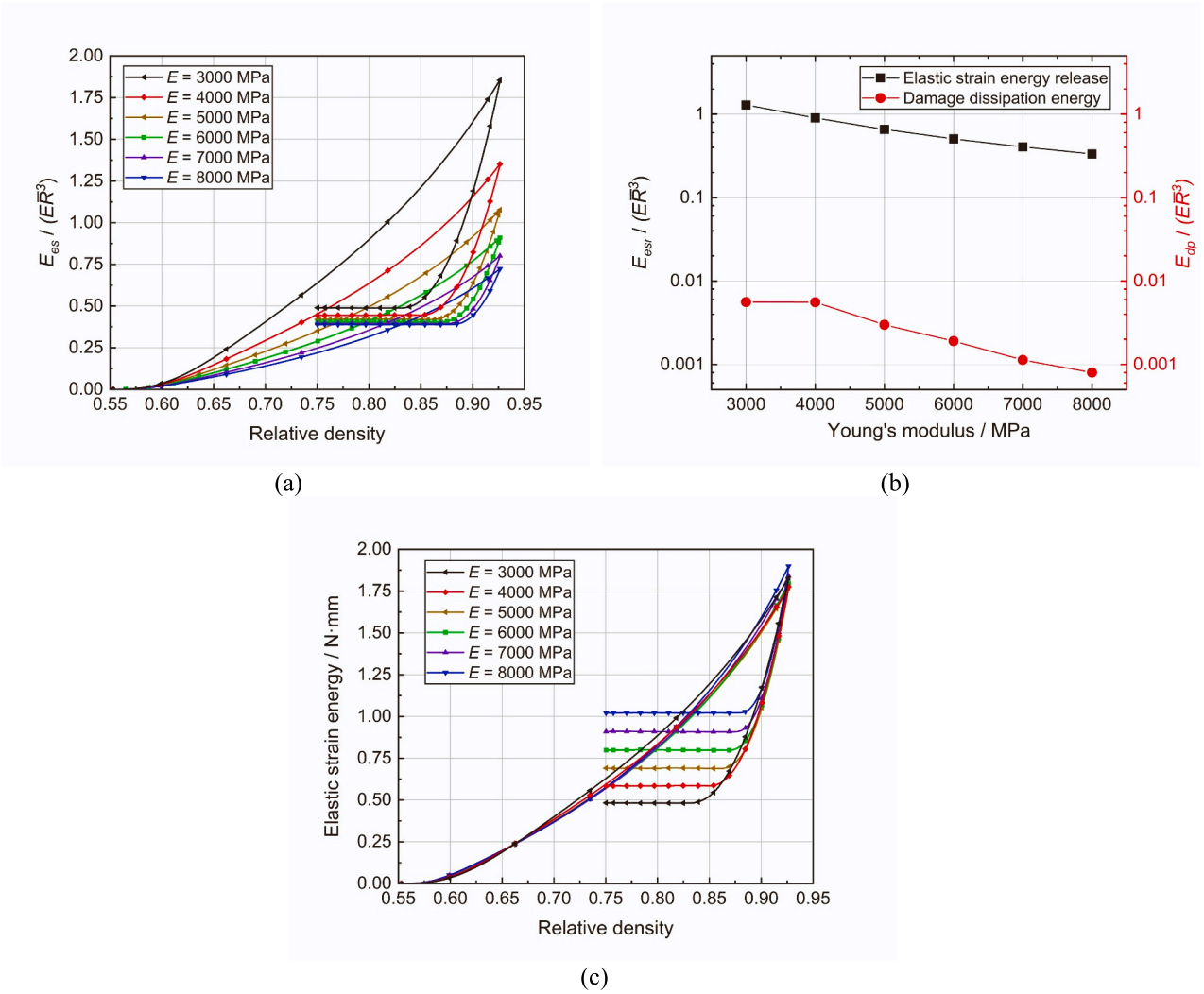

Fig. 11. Evolution of elastic strain energy of the system during the loading and unloading stages. (a) Variation of the release of elastic strain energy and the total damage dissipation energy with Young's modulus of grains during the unloading process. Variation of the elastic strain energy without normalization of the system during the loading (b) and unloading (c) stages.

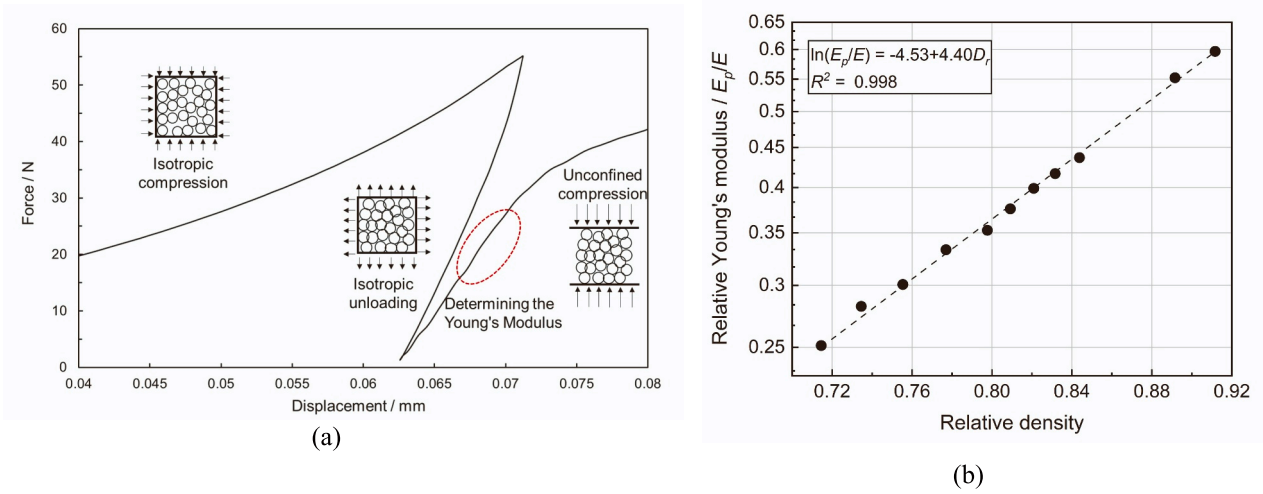

Fig. 12. (a) Illustration of a typical three-stage loading to determine the Young's modulus of a powder assembly after elastic recovery. (b) Correlation between the maximum relative density and the normalized Young's modulus.

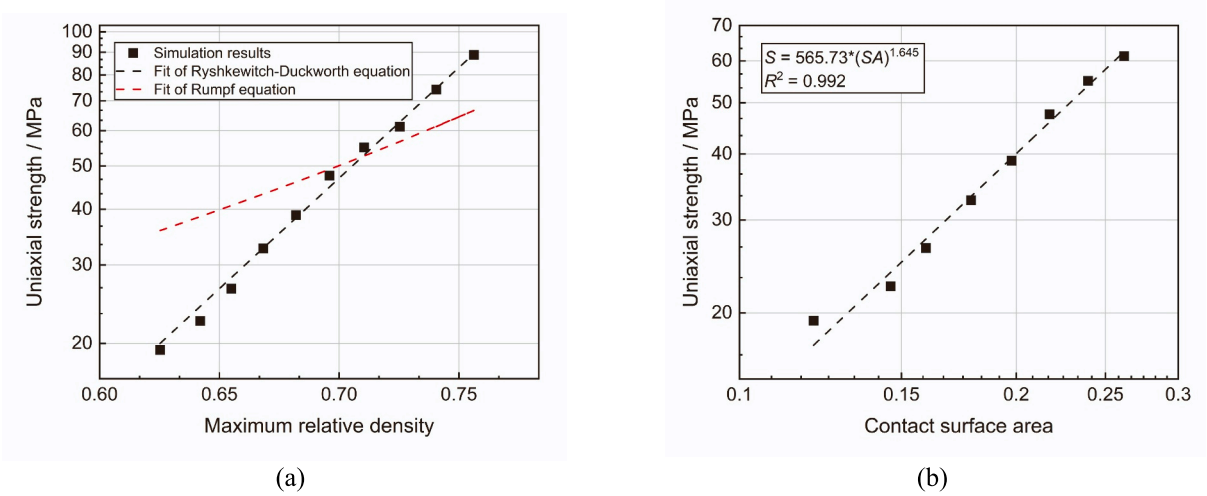

Fig. 13. Variation of uniaxial strength of isotropically compacted powders with maximum relative density (a) and contact surface area (b).

Also affecting the unconfined strength of the compacted assembly is the total contact area between grains. The strength of the cohesion and the contact surface area over which these bonds are active are two critical influence factors in determining the strength of tablets [55]. The use of mesh based multi-particle finite element method in this study facilitates easy quantification of the contact surface area. The contact surface area in Fig. 13(b) refers to the ratio of the contacted area between grains to their total surface area. A linear correlation between the contacted area and the crushing strength is in double logarithmic plots as is shown in Fig. 13(b) is found. Both correlations reveal a strong

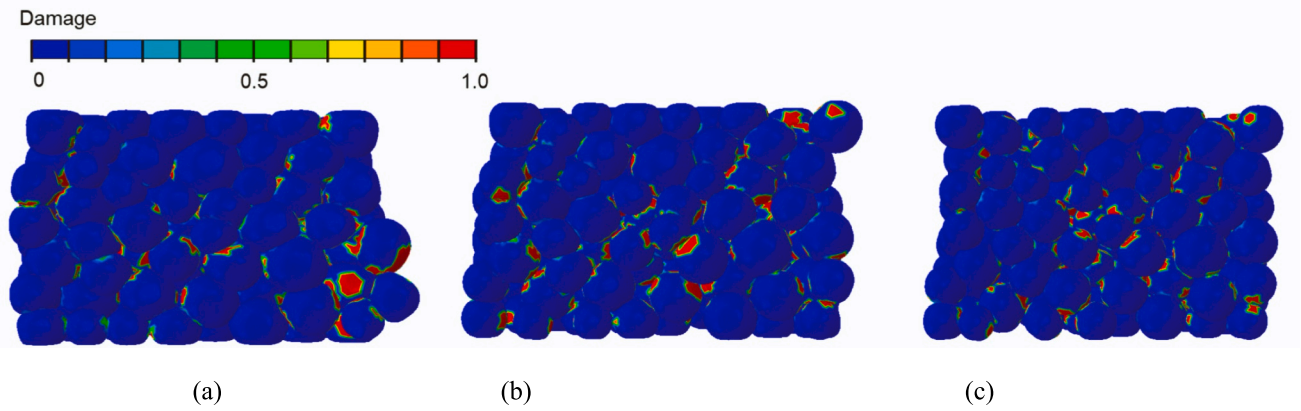

Fig. 14. Damage pattern with three different maximum relative densities: 0.73 (a), 0.67 (b), and 0.63 (c).

coupling effect of cohesive bonds and plastically deformed contacts in dictating the uniaxial strength of a compacted powder assembly. Fig. 14 further illustrated the damage patterns at the peak of the loading curves of cases for three different D_r^{max}. Under uniaxial compression, the powder assembly may experience shear failure like damage at the inter-particle bonds which result in successive fractures propagating from top boundary to the bottom.

It is instructive to further explore how the Young's modulus and the uniaxial strength correlate with the bond strength. Fig. 15 shows the loading curves for different fracture energies of cohesive contact when determining the crushing strength. Fig. 16(a) shows the correlated increase of the Young's modulus of assembly with G^c according to an inverse exponential fitting. The trend in Young's modulus with G^c is consistent with the experiments. An experimental study by Yeheskel et al. [87] confirms the increase in elastic moduli and bond strength of discrete porous copper and thus stiffer structure due to cold compaction or sintering. The Young's modulus may converge to a saturated value of 2312.73 MPa beyond which further increase in G^c will not lead to changes in its value. Note that when the maximum relative density is close to 1.0 in conjunction with a sufficiently large G^c (e.g., beyond the saturation threshold), the Young's modulus of a powder assembly is supposed to be close to that of the individual grains. The fitted line in Fig. 12(b) does not go through point $E_p/E = 1$ and $P = 0$. The presence of bond damage may play a role in dictating this behavior. Note that the bond strength also affects the uniaxial strength critically which is presented in Fig. 16(b). Interestingly, both the relative density of packing and the fracture energy of cohesion have similar effects on the elastic and damage behavior. For example, the fitted curves in Figs. 12(b) and 13(a) share a similar correlation with maximum relative density, as are the fitted curves in Fig. 16 (a) and (b). The presence of cohesion may play a key role in the observations of the Young's modulus and the uniaxial compressive strength of the packing.

4.3. Behavior under triaxial compression

It is instructive to explore the mechanical response of a compacted powder assembly under triaxial compression. Similar procedures are followed to prepare the compacted assembly by isotropically compressing an assembly of powders to a specific D_r^{max} before unloaded isotropically to a certain confining pressure. In this study, the forces applied to lateral rigid walls of the specimen are kept constant, while the sample is compressed axially until failure. The mechanical parameters used here are shown in Table 1. Fig. 17 depicts the stress path in the p-q plane during a typical isotropic compression, isotropic unloading, and triaxial compression. The lateral walls are supported by constant concentrated force in our simulations to render an approximate confining pressure of 8 MPa. The stress state at 15% axial strain is selected as the triaxial compression strength when there is no apparent peak for the triaxial loading curve in the p-q plane.

Fig. 18 presents the stress-strain responses and dilation curve during triaxial compression of powders previously isotropically compressed to different D_r^{max}. Evidently, all cases under consideration show a hardening behavior under triaxial compression, with higher D_r^{max} case showing a higher deviator stress and steady state strength. A trend of volumetric contraction is found for all cases in Fig. 18 (b). The smaller the maximum relative density of the sample during isotropic loading, the greater the volumetric contraction is found during triaxial compression. This suggests that the packing may still undergo densification during the triaxial compression. Fig. 19(a) and (b) show the damage and plastic dissipated energy during the triaxial compression, respectively. The effect of maximum relative density is similar for both damage and plastic dissipated energy. When D_r^{max} increases, due to the larger contact area and closer contact between the particles, a packing may have a greater damage dissipated energy and more plastic deformation during triaxial compaction.

Similar to the uniaxial case, the powder bond cohesion also affects triaxial mechanical properties. Fig. 20 presents the mechanical responses of powder assemblies compacted with different G^c before undergoing triaxial compression with a constant confining pressure of 8 MPa. Except G^c, all mechanical parameters adopt those listed in Table 1. The maximum relative density D_r^{max} is sets to 0.92 for all cases. The higher G^c cases generally show a hardening stress-strain relation, whereas lower G^c cases exhibit an apparent peak followed by a softening stage. Lower G^c leads to lower peak deviatoric stress which occurs at an earlier axial strain level. It appears that the bond cohesion G^c plays such a role as to changing the shear behavior of a powder assembly from "granular-like" rheology (with a peak and a softening) at low G^c to "plasticity-dominant" rheology (with a steady flow at high shear deformation) at high G^c. The mechanical behavior of packing gradually changes from a granular-like material to a porous plastic material as G^c becomes larger.

Compared to the influence of D_r^{max} in Fig. 18, it is indicative that

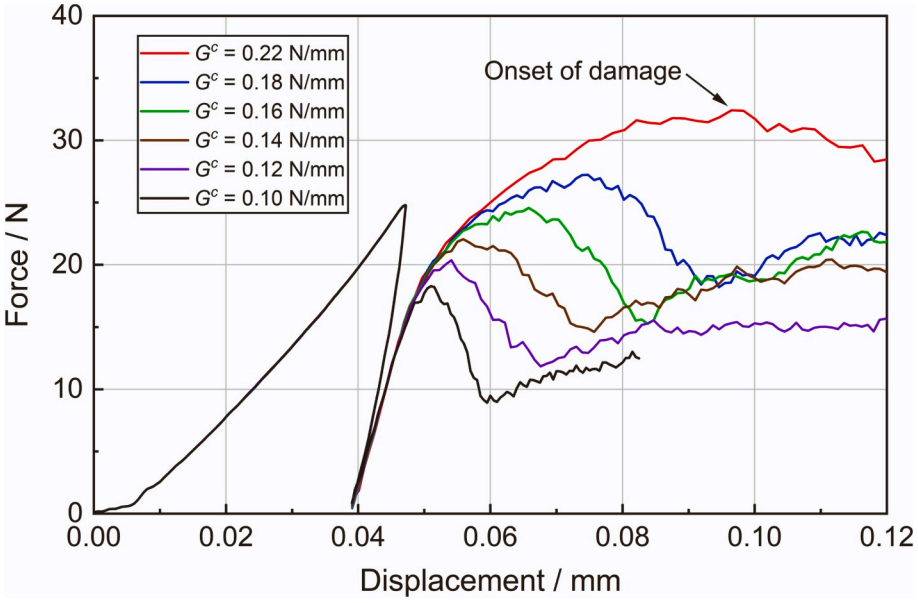

Fig. 15. Force and displacement curves of the upper plate for different G^c.

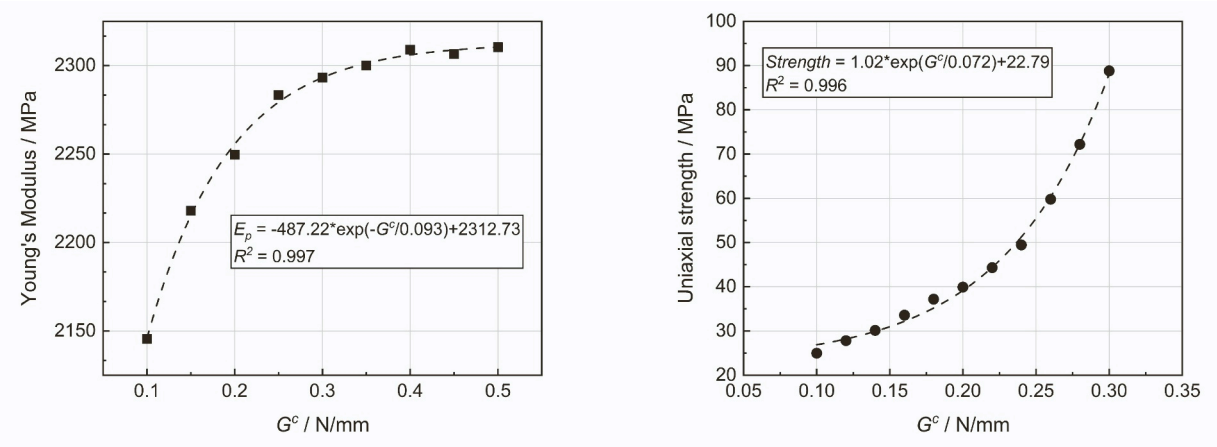

Fig. 16. Relation between Young's modulus and the fracture energy G^c (a), and the relation between uniaxial strength and the fracture energy G^c.

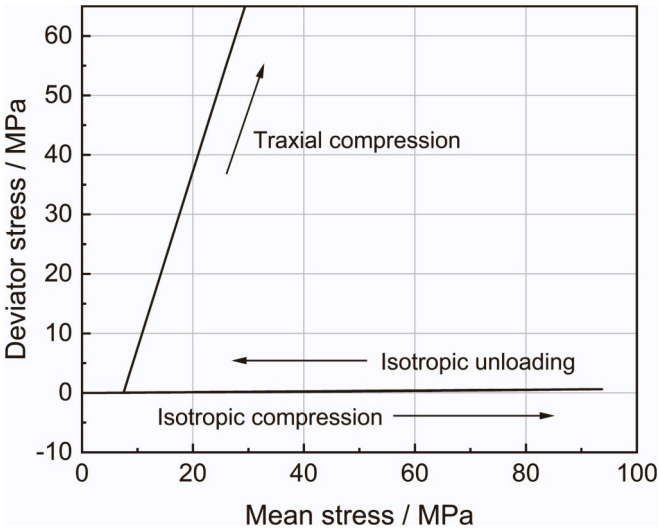

Fig. 17. Stress paths in triaxial compression processes.

reducing the strength of the bond cohesion is more likely to produce softening than reducing the targeted D_r^{max}. The dilation curve in Fig. 20 (b) shows a quicker switch from instant contraction to significantly more dilative behavior in the low or no G^c cases. The presence of stronger G^c between powder grains helps to prolong the contraction stage before reaching a less dilative state at large shear flow. The more dilative behavior of the low G^c case may also be attributable to the more significant damage of cohesion (shown in Fig. 21), which allows more particle rearrangement for an already dense assembly.

It becomes evident that the triaxial compression strength of a compacted powder assembly may be a function of both confining pressure and bond strength G^c. Based on our simulation data, the following exponential law relation can be fitted between the deviator strength and the confining pressure and G^c which is further is depicted in Fig. 22:

$$q = 89.93 - 73.64exp(P_c/7.51)exp(-G^c/0.11) \quad (13)$$

The correlation is performed with a coefficient $R^2 = 0.978$. The deviator strength increases with both the confining pressure p_c and G^c. The projections of the 3D correlation surface are also shown in Fig. 22. To clearly show the results, we only selected the results of $p_c = 8$ MPa and G^c equal to 0.5 N/mm, 0.1 N/mm and 0 to be projected on the corresponding plane. For different P_c and G^c, the projected points on

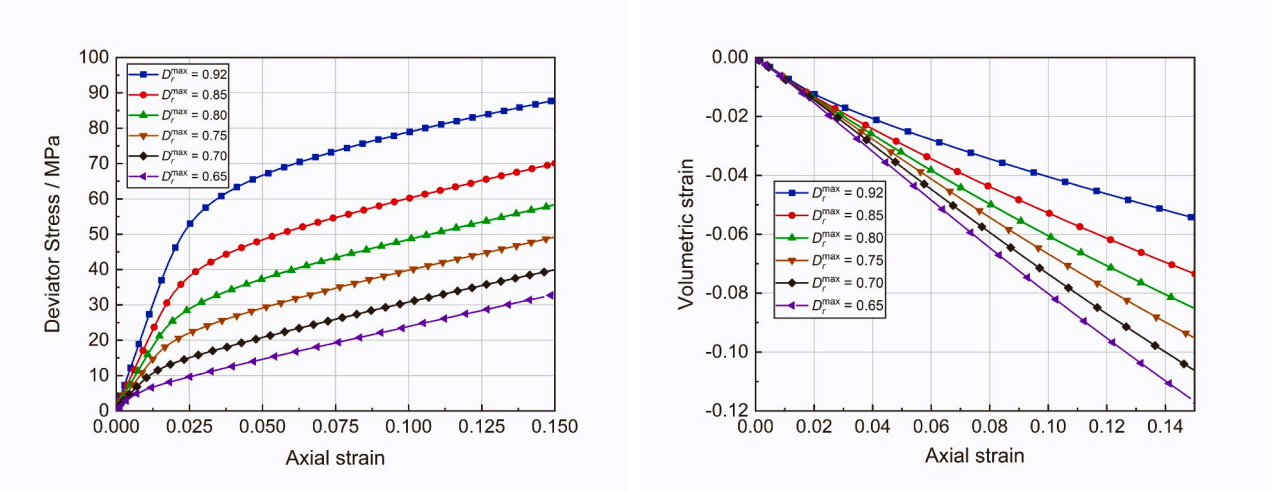

Fig. 18. Simulation results for different maximum relative densities and the same G^c equal to 0.5 N/mm (a) Deviator stress vs axial strain with different relative density, and (b) volumetric strain vs axial strain with different relative density.

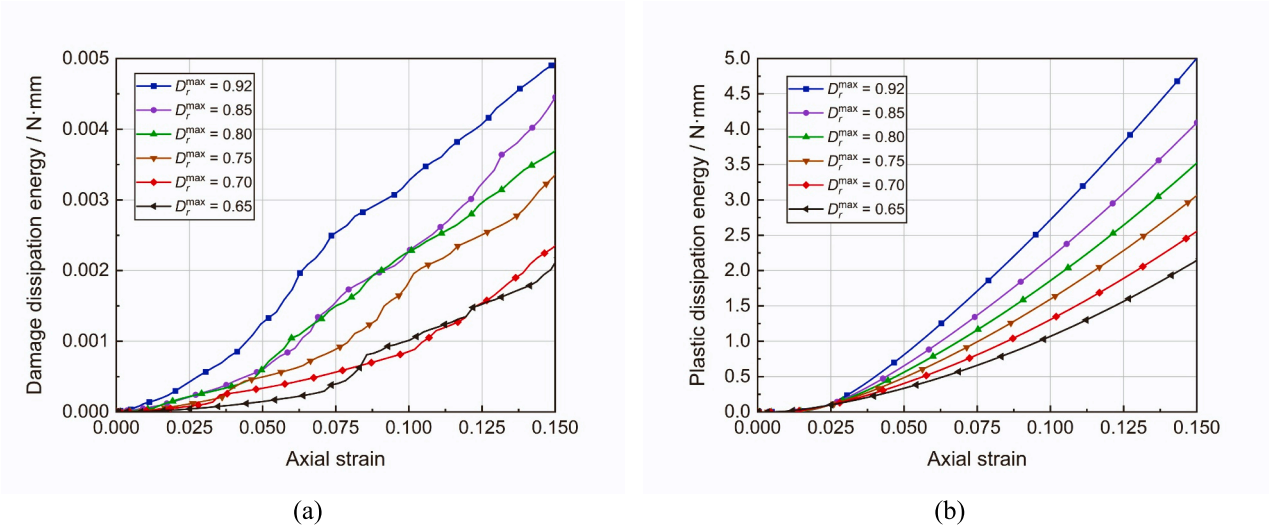

Fig. 19. (a) Damage dissipated energy during triaxial compression with different maximum relative densities; (b) plastic dissipated energy during triaxial compression with different maximum relative densities.

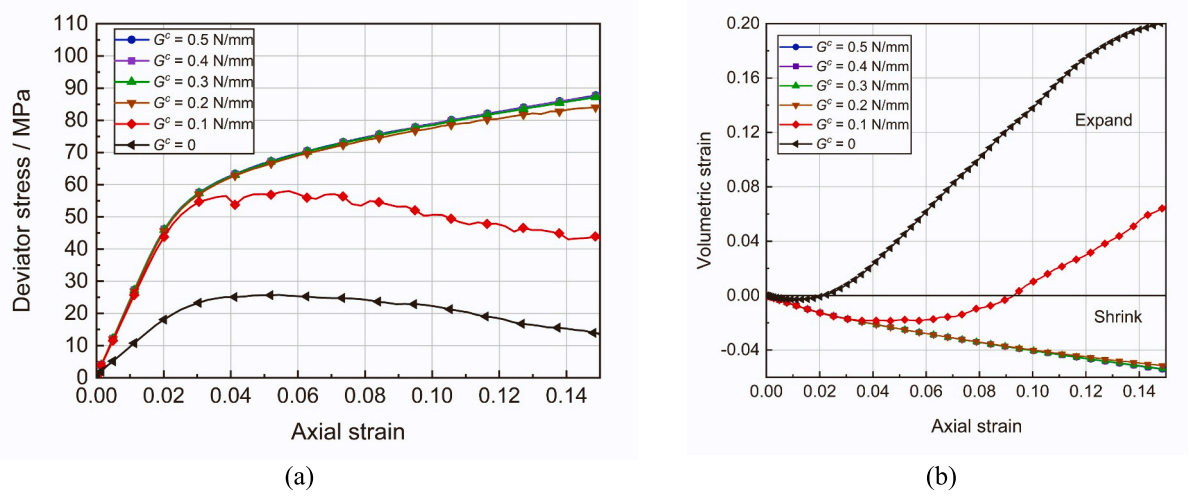

Fig. 20. Deviator stress vs. axial strain with different G^c (a) and volumetric strain vs. axial strain with different G^c (b).

both mean stress and deviatoric stress plane and G^c- deviatoric stress are found to fit an exponential law well.

4.4. Yielding

It is critical to understand the yielding behavior of compacted powders. Energy dissipation has been commonly used in numerical studies to determine the onset of plasticity of a powder system. Indeed, Schmidt et al. [68] proposed an energy-based approach to examine the energy dissipated through plastic deformation and frictional sliding during the compaction of powders. As illustrated in Fig. 23(a), the identification of yielding typically involve stress path probes consisting of isotropic loading (1), isotropic unloading (2), and anisotropic reloading (3), to determine the yield surface in a mean stress-deviatoric stress space (or *p-q* space). During such a probing stress path, the total (accumulated) energy dissipation is illustrated in Fig. 23(b) where it is assumed no energy dissipation presents during the small, purely elastic unloading stage (energy dissipation may occur if the unloading to a low stress state) and yielding occurs during the reloading stage. Following Schmidt et al. [68], the onset of yielding is identified by a point during the reloading stage where the total dissipated energy amounts to 1.003 times of that at the end of the unloading stage. Note that this study considers energy dissipation of both plastic and damage mechanisms due to the presence of cohesive bond.

Following the above probing protocol, a powder assembly is first isotropically compacted to a maximum relative density $D_r^{max} = 0.92$ at the end of the loading stage (1) and unloaded to a pressure of 60 MPa before different probing paths in both compression (positive q) and extension mode (negative q) modes. The identified yield surface is plot it in the *p-q* plane in Fig. 24 against a comparison case with no cohesion ($G^c = 0$) considered (e.g., only plastic yielding occurs). Notably, the no-cohesion case presents a yield surface smaller than that with cohesion at the high mean stress regime. The high confinement apparently facilitates the formation of cohesion in the cohesive powder case which further contributes to the higher yielding of the assembly.

Since the rigid non-adhesive loading plate is considered in this study, only half of the yielding surface can be presented here. However, it can be reasonably inferred from the present yield surface that the cohesive powders may possess a lower yielding stress than its no-cohesion counterpart in the low mean stress regime. The combined mechanism of plasticity and cohesive bond damage accounts for this observation in our study. The weakly formed cohesion at lower confinements may not offer sufficient resistance to uniaxial compression and hinder the rearrangements of powder grains to form optimal packing as no-cohesion

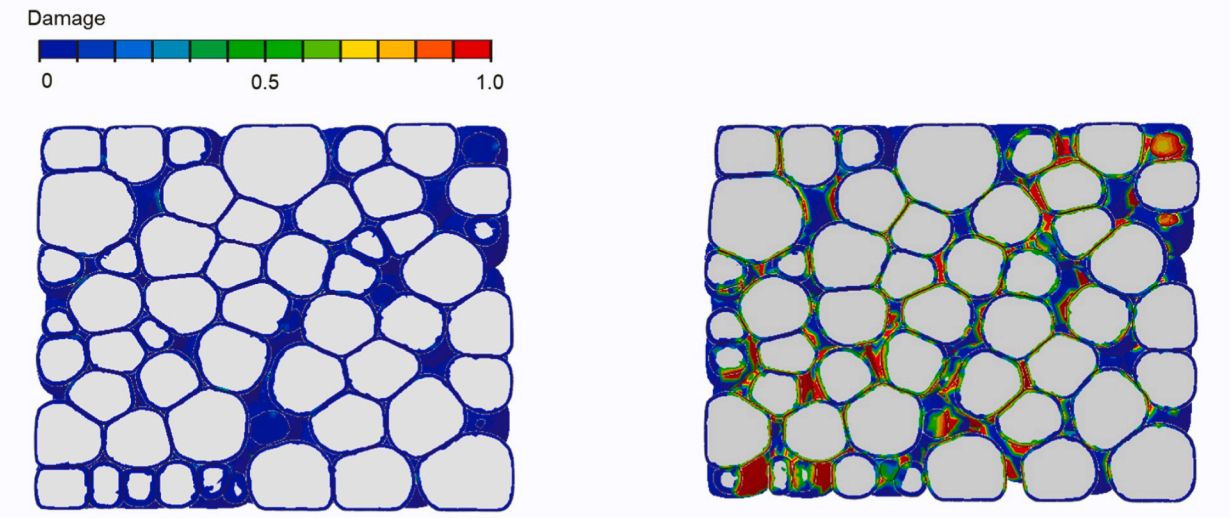

Fig. 21. Cohesion damage profile at axial strain of 0.15 for the model case $D_r^{max} = 0.92$ at middle cross section during triaxial loading with: (a) $G^c = 0.5$ N/mm, (b) $G^c = 0.1$ N/mm.

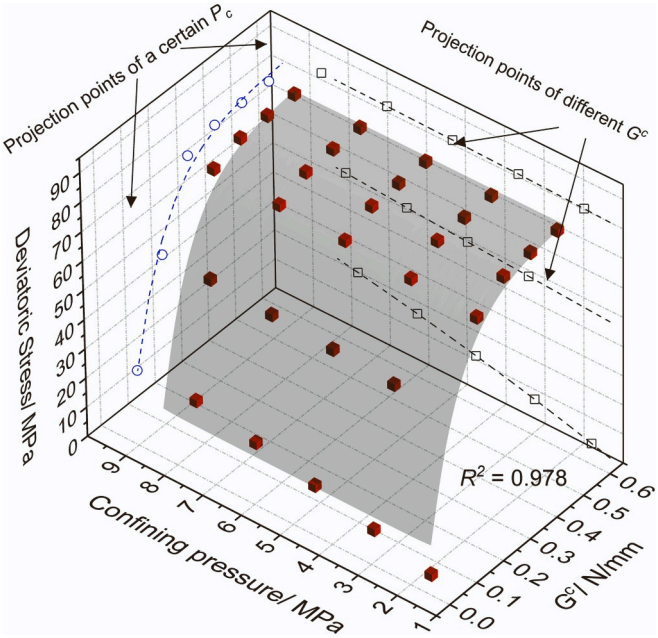

Fig. 22. Relationship between the deviator stress, the confining pressure, and the fracture energy.

case does during the compaction stage, which may provide an explanation on the above observation. Note that Schmidt et al. [69] found the yielding surface is larger in higher frictional coefficient than lower case in all stress regimes where they considered a combined mechanism of plasticity and friction. The different roles played by interparticle friction and cohesion in highly deformable powders are interesting. For the cases treated by Schmidt et al. [69], plasticity and friction may play a comparable role in the dissipation (it certainly depends on the loading conditions, e.g., shear loading or compaction loading). However, the presence of cohesion may restrain the motions of powder grains, rendering the plastic deformation become major contributor to energy dissipation. Our numerical results (not presented here) also indicate the damage dissipation due to debonding constitutes only a marginal portion of the total energy dissipation which is dominated by plastic deformation mechanism. Indeed, Mollon [49] investigated the shear behavior of elastic cohesive particles and found the cohesion may play a role changing the flow regime and the associated modes of energy dissipation. For example, it may help switch the dominant contributor of dissipation from the contacts between two grains to the inelastic deformation within these grains.

4.5. Compaction hysteresis

The hysteresis behavior of compacted powders under cyclic loading serves important reference for understanding the quality of compaction. We herein consider cyclic load under isotropic compaction and unloading. Fig. 25 shows the hysteresis curves for both cases with and without cohesion with other model parameters adopted according to Table 1. Cyclical loading with a mean stress between the mean stress of 0.5 MPa and 85 MPa is applied to the packing where force-controlled boundary conditions are prescribed.

It is interesting to observe that the nonlinear hysteresis loop of the cohesive sample exhibits a gradual left shifting (or to the looser side) during the cyclic loading, whereas it shifts to the right (the denser side) for the case without cohesion. The observed difference stems precisely from the presence of cohesive bonds that changes the powder motion, stress redistribution, elastoplastic deformation, and energy dissipation. Note that no friction is considered in either case. In the case of cohesive powders, the establishment of cohesive bonds during the compaction stage of each loading cycle serves as effective constraints to the free motion of powder particles and hence hinder stress redistribution of the entire assembly. The severely deformed particles cannot adequately rebound to allow energy release. Instead, the entire assembly must dissipate significant portion of the energy through plastic deformation. This can be better elaborated by Fig. 26 where the energies dissipated by the damage process of debonding Fig. 26(a) and plastic dissipation Fig. 26(b) during the load cycle are shown. It appears that the energy spent through plastic dissipation is dominant in a cohesive powder assembly, amounts to three magnitudes of order to that dissipated through damage of cohesive bond. The no cohesion case also shows roughly twice as much of plastic dissipation as compared to the cohesive case in Fig. 26(b). Since interparticle friction is not considered in this study, the no cohesion case represents an idealized situation where more free particle rearrangements are allowed without the constraints of cohesion or friction. Consequently, adequate stress redistributions are permitted

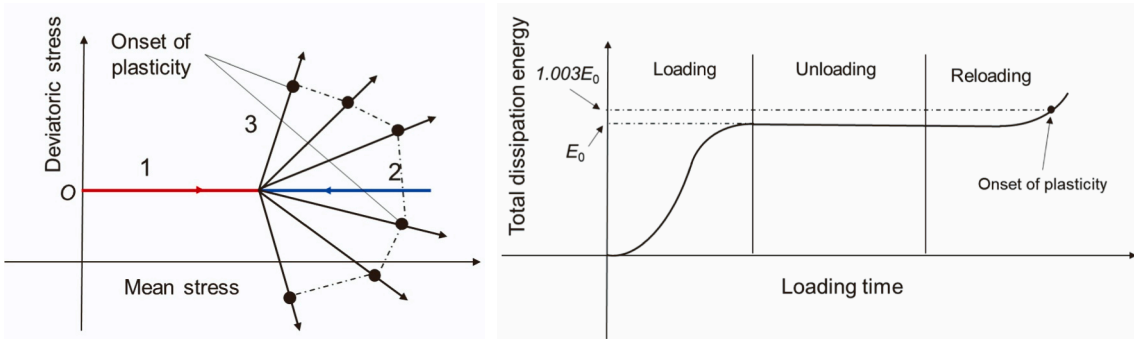

(a) (b)

Fig. 23. Stress path diagram (a), the dissipated energy criterion to determine the onset of plasticity (b).

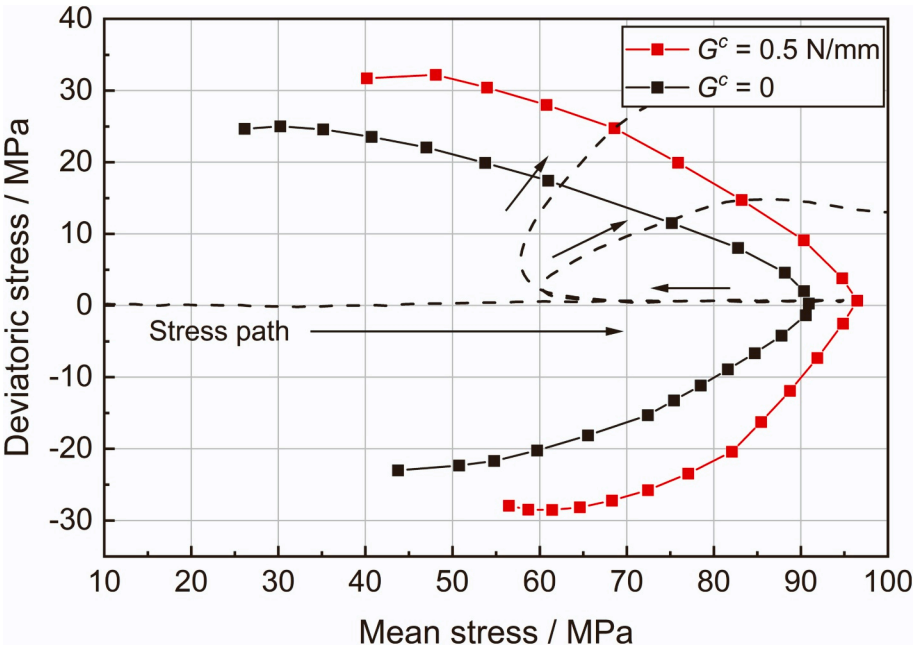

Fig. 24. The yield surface of the assembly with and without cohesive contact.

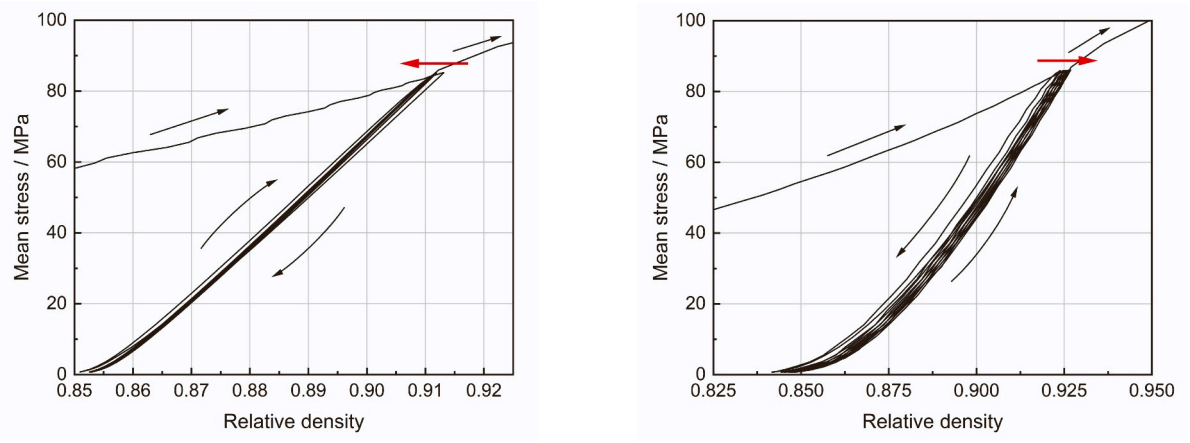

(a) (b)

Fig. 25. Hysteresis loading curves for powder assemblies with cohesive contact (a) and without cohesive contact (b) subjected to cyclic isotropic compaction and unloading.

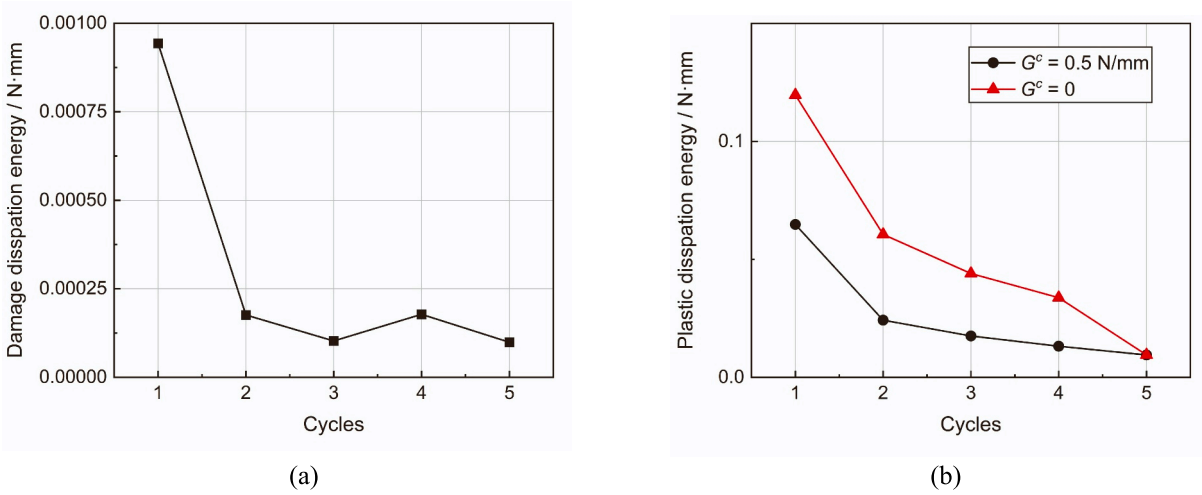

Fig. 26. Variation of damage dissipation energy per-cycle (a) and plastic dissipation energy per-cycle (b) with cycle number.

in the assembly to increase plastic dissipation in the assembly. The rightward shifting of the cyclic loading curve and larger loop area indicate more work being done on the packing by external force than in the presence of cohesion. The extra work may result in more plastic dissipated energy of the packing. Nevertheless, the plastically deformed particles may introduce non-spherical shape effect as compared to their initial spherical shapes to gradually cause dilation in the assembly during the loading cycles. This explains the gradual left-ward shifting of the cyclic loading curve in Fig. 26(a). In either case, the plastic dissipation generation drops with the loading cycles to reach a steady state.

5. Conclusions

A multi-particle finite element method (MPFEM) in conjunction with a cohesive contact model was developed to simulate the compaction of cohesive, plastic granular powders. The theoretical and numerical models were rigorously validated before being applied to systematically examine the elastic and plastic, yielding, damage, and hysteresis behaviors of granular powders subjected to different loading and unloading conditions. The results and findings help to shed new insight into deeper understanding of the compaction mechanism of cohesive, deformable granular powders relevant to their engineering and industrial performance such as in pharmaceutical and chemical engineering. Major conclusions drawn from the study are summarized as follows:

(1) The elastic behavior of compacted powder assembly, in terms of elastic recovery and relative elastic modulus, is highly dependent on the targeted maximum relative density and the Young's modulus of individual powder grains. Elastic recovery is found to be linearly proportional with the maximum relative density and presents an inverse linear correlation with the Young's modulus of the powder grain on a semi-log plot. The Young's modulus of compacted packing increases exponentially with the maximum relative density the powders are compacted to, confirming a previous experimentally based empirical relation.
(2) The designated maximum relative density serves as an important index deciding the overall performance of a compacted powder assembly. Both unconfined compressive strength and triaxial compression strength of the compacted assembly are found positively correlated with the relative density according to an exponential law.
(3) The inter-particle cohesion plays a key role in affecting the deformation, yielding and failure of compacted powders by altering the coupling mechanisms among elastic and plastic behavior, debonding, and energy dissipations, as compared to a no-cohesion case. Our study provides quantitative correlations between inter-particle cohesion with macroscopic indexes including unconfined and triaxial strength, Young's modulus and energy dissipations through both bond damage and plastic deformation.
(4) The bond strength and the plastic behavior of the powder grains are coupled in affecting the overall behavior of the compaction of powders.

Notably, the current study has been limited to deformable powder grains which can develop cohesion, without consider inter-particle friction. Friction, serve as a representative feature of granular media, may affect the compaction and post-compaction behavior in conjunction with inter-particle cohesion and plastic deformation. This study has placed a focus on the behavior of Microcrystalline Cellulose (MCC) 102 powders based on one set of parameters. The strength of cohesion was varied to examine the properties of the MCC compact, based on which new insights into the behavior of powder compaction were drawn. Notably, however, different particulate materials may vary in physical properties. As such, the conclusions drawn from this study may not be generally applicable to all powders. More systematic studies are needed to verify the general validation of these conclusions in the future. Meanwhile, all numerical simulations in the study have been performed on the element mesoscale for the purpose of mechanism study. To understand the performance of a compacted powder assembly under more realistic boundary conditions, simulating it as a boundary value problem in full consideration of the boundary effect near the loading plate, possible element distortion and localized failure due to large deformation may be needed. These will be tackled in the future. Note also that the present study has been focused to understand the fundamental behavior of highly deformable cohesive powders from a micro-mechanical point of view. It may not be ready to provide recommendations that are immediately useful for industries without further work on large scale simulations with more complex boundary conditions. Therefore, the presented results are intended to offer new micro-mechanical insights for researchers in the field to develop better constitutive models or multi-scale computational methods to investigate industrial level behavior of powder compaction in the future.

CRediT authorship contribution statement

Quan Ku: Conceptualization, Methodology, Software, Investigation, Writing – original draft. **Jidong Zhao:** Conceptualization, Methodology, Writing – original draft, Writing – review & editing, Supervision, Funding acquisition, Project administration. **Guilhem Mollon:** Writing

– review & editing. **Shiwei Zhao:** Writing – review & editing.

Declaration of Competing Interest

The authors declare that they have no known competing financial interests or personal relationships that could have appeared to influence the work reported in this paper.

Data availability

No data was used for the research described in the article.

Acknowledgments

The study was financially supported by National Natural Science Foundation of China (under Project 11972030), Research Grants Council of Hong Kong (GRF #16208720, F-HKUST601/19), and the Project of Hetao Shenzhen-Hong Kong Science and Technology Innovation Cooperation Zone (HZQB-KCZYB-2020083). JZ aknowledges the internal research supports provided by HKUST (via projects IEG22EG01 and FP907). QK wishes to acknowledge helpful discussion with Dr. Deheng Wei of RWTH Aachen University.

References

[1] Abaqus, Analysis User's Manual, 2020.
[2] N. Abdelmoula, B. Harthong, D. Imbault, P. Dorémus, A study on the uniqueness of the plastic flow direction for granular assemblies of ductile particles using discrete finite-element simulations, Journal of the Mechanics and Physics of Solids 109 (2017) 142–159.
[3] A. Baroutaji, K. Bryan, M. Sajjia, S. Lenihan, Mechanics and computational modeling of pharmaceutical tabletting process, in: Reference Module in Materials and Materials Engineering, Elsevier, 2017, pp. 1–10.
[4] F. Bassam, P. York, R.C. Rowe, R.J. Roberts, Young's modulus of powders used as pharmaceutical excipients, Int. J. Pharm. 64 (1) (1990) 55–60.
[5] W. Bier, M.P. Dariel, N. Frage, S. Hartmann, O. Michailov, Die compaction of copper powder designed for material parameter identification, Int. J. Mech. Sci. 49 (6) (2007) 766–777.
[6] P.P. Camanho, C.G. Dávila, Mixed-mode decohesion finite elements for the simulation of delamination in composite materials, in: Technical Memorandum, NASA/TM-2002-211737, NASA, 2002.
[7] D. Cantor, M. Cárdenas-Barrantes, I. Preechawuttipong, M. Renouf, E. Azéma, Compaction model for highly deformable particle assemblies, Phys. Rev. Lett. 124 (20) (2020), 208003.
[8] M. Cárdenas-Barrantes, D. Cantor, J. Barés, M. Renouf, E. Azéma, Three-dimensional compaction of soft granular packings, Soft Matter 18 (2) (2022) 312–321.
[9] S. Carlsson, S. Biwa, P.L. Larsson, On frictional effects at inelastic contact between spherical bodies, Int. J. Mech. Sci. 42 (1) (2000) 107–128.
[10] M.A. Cooper, M.S. Oliver, D.C. Bufford, B.C. White, J.B. Lechman, Compression behavior of microcrystalline cellulose spheres: single particle compression and confined bulk compression across regimes, Powder Technol. 374 (2020) 10–21.
[11] O. Coube, A.C.F. Cocks, C.Y. Wu, Experimental and numerical study of die filling, powder transfer and die compaction, Powder Metall. 48 (1) (2005) 68–76.
[12] P.A. Cundall, O.D. Strack, A discrete numerical model for granular assemblies, Geotechnique 29 (1) (1979) 47–65.
[13] B.W. Darvell, Uniaxial compression tests and the validity of indirect tensile strength, J. Mater. Sci. 25 (2) (1990) 757–780.
[14] A. Demirtas, G.R. Klinzing, Understanding die compaction of hollow spheres using the multi-particle finite element method (MPFEM), Powder Technol. 391 (2021) 34–45.
[15] P.J. Denny, Compaction equations: a comparison of the Heckel and Kawakita equations, Powder Technol. 127 (2) (2002) 162–172.
[16] H. Diarra, V. Mazel, A. Boillon, L. Rehault, V. Busignies, S. Bureau, P. Tchoreloff, Finite element method (FEM) modeling of the powder compaction of cosmetic products: comparison between simulated and experimental results, Powder Technol. 224 (2012) 233–240.
[17] R.D. Domike, Pharmaceutical Powders in Experiment and Simulation: Towards a Fundamental Understanding (Doctoral dissertation,, Massachusetts Institute of Technology, 2004.
[18] M. Duberg, C. Nyström, Studies on direct compression of tablets XVII. Porosity—pressure curves for the characterization of volume reduction mechanisms in powder compression, Powder Technol. 46 (1) (1986) 67–75.
[19] D. Farkas, Atomistic studies of intrinsic crack-tip plasticity, MRS Bull. 25 (5) (2000) 35–38.
[20] G. Frenning, Compression mechanics of granule beds: a combined finite/discrete element study, Chem. Eng. Sci. 65 (8) (2010) 2464–2471.
[21] D.T. Gethin, R.S. Ransing, R.W. Lewis, M. Dutko, A.J.L. Crook, Numerical comparison of a deformable discrete element model and an equivalent continuum analysis for the compaction of ductile porous material, Comput. Struct. 79 (13) (2001) 1287–1294.
[22] M. Gonzalez, Generalized loading-unloading contact laws for elasto-plastic spheres with bonding strength, Journal of the Mechanics and Physics of Solids 122 (2019) 633–656.
[23] M. Gonzalez, A.M. Cuitiño, A nonlocal contact formulation for confined granular systems, Journal of the Mechanics and Physics of Solids 60 (2) (2012) 333–350.
[24] M. Gonzalez, A.M. Cuitiño, Microstructure evolution of compressible granular systems under large deformations, Journal of the Mechanics and Physics of Solids 93 (2016) 44–56.
[25] F. Güner, Ö.N. Cora, H. Sofuoğlu, Effects of friction models on the compaction behavior of copper powder, Tribol. Int. 122 (2018) 125–132.
[26] G. Gustafsson, H.Å. Häggblad, P. Jonsén, Multi-particle finite element modelling of the compression of iron ore pellets with statistically distributed geometric and material data, Powder Technol. 239 (2013) 231–238.
[27] P. Han, X. An, Y. Zhang, F. Huang, T. Yang, H. Fu, Z. Zou, Particulate scale MPFEM modeling on compaction of Fe and Al composite powders, Powder Technol. 314 (2017) 69–77.
[28] B. Harthong, D. Imbault, P. Dorémus, The study of relations between loading history and yield surfaces in powder materials using discrete finite element simulations, Journal of the Mechanics and Physics of Solids 60 (4) (2012) 784–801.
[29] B. Harthong, J.F. Jérier, P. Dorémus, D. Imbault, F.V. Donzé, Modeling of high-density compaction of granular materials by the discrete element method, Int. J. Solids Struct. 46 (18–19) (2009) 3357–3364.
[30] A. Hattiangadi, A. Bandyopadhyay, Strength degradation of nonrandom porous ceramic structures under uniaxial compressive loading, J. Am. Ceram. Soc. 83 (11) (2000) 2730–2736.
[31] R.V. Haware, I. Tho, A. Bauer-Brandl, Application of multivariate methods to compression behavior evaluation of directly compressible materials, Eur. J. Pharm. Biopharm. 72 (1) (2009) 148–155.
[32] R.W. Heckel, Density-pressure relationships in powder compaction, Trans. Metall. Soc. AIME 221 (4) (1961) 671–675.
[33] M.L. Hentschel, N.W. Page, Elastic properties of powders during compaction. Part 1: Pseudo-isotropic moduli, J. Mater. Sci. 42 (4) (2007) 1261–1268.
[34] Y. Hiramatsu, Y. Oka, Determination of the tensile strength of rock by a compression test of an irregular test piece, International Journal of Rock Mechanics and Mining Sciences & Geomechanics Abstracts 3 (2) (1966) 89–90. Pergamon.
[35] G. Hu, B. Zhou, R. Fu, Y. Guo, C. Han, K. Lv, Discrete element modeling of the compression molding of polymer–crystal composite particles, Powder Technol. 390 (2021) 112–125.
[36] J.F. Jerier, B. Hathong, V. Richefeu, B. Chareyre, D. Imbault, F.V. Donze, P. Doremus, Study of cold powder compaction by using the discrete element method, Powder Technol. 208 (2) (2011) 537–541.
[37] Q. Jia, X. An, H. Zhao, H. Fu, H. Zhang, X. Yang, Compaction and solid-state sintering of tungsten powders: MPFEM simulation and experimental verification, J. Alloys Compd. 750 (2018) 341–349.
[38] K.L. Johnson, K. Kendall, A. Roberts, Surface energy and the contact of elastic solids, Proceedings of the Royal Society of London. A. Mathematical and Physical Sciences 324 (1558) (1971) 301–313.
[39] K. Kawakita, K.H. Lüdde, Some considerations on powder compression equations, Powder Technol. 4 (2) (1971) 61–68.
[40] H.L. Keizer, P. Kleinebudde, Elastic recovery in roll compaction simulation, Int. J. Pharm. 573 (2020), 118810.
[41] A.R. Khoei, A.R. Sameti, H. Mofatteh, Compaction simulation of crystalline nano-powders under cold compaction process with molecular dynamics analysis, Powder Technol. 373 (2020) 741–753.
[42] S.P. Kiselev, Compaction of a mixture of copper and molybdenum nanopowders modeled by the molecular dynamics method, J. Appl. Mech. Tech. Phys. 49 (2008) 712–722.
[43] G. Ma, Y. Chen, F. Yao, W. Zhou, Q. Wang, Evolution of particle size and shape towards a steady state: insights from FDEM simulations of crushable granular materials, Comput. Geotech. 112 (2019) 147–158.
[44] A.B. Mashadi, J.M. Newton, The characterization of the mechanical properties of microcrystalline cellulose: a fracture mechanics approach, J. Pharm. Pharmacol. 39 (12) (1987) 961–965.
[45] A.E. Mayer, A.A. Ebel, M.K. Al-Sandoqachi, Plastic deformation at dynamic compaction of aluminum nanopowder: molecular dynamics simulations and mechanical model, Int. J. Plast. 124 (2020) 22–41.
[46] S.D. Mesarovic, K.L. Johnson, Adhesive contact of elastic-plastic spheres, Journal of the Mechanics and Physics of Solids 48 (10) (2000) 2009–2033.
[47] M. Moghaddam, R. Darvizeh, K. Davey, A. Darvizeh, Scaling of the powder compaction process, Int. J. Solids Struct. 144 (2018) 192–212.
[48] G. Mollon, Mixture of hard and soft grains: micromechanical behavior at large strains, Granul. Matter 20 (3) (2018) 1–16.
[49] G. Mollon, Solid flow regimes within dry sliding contacts, Tribol. Lett. 67 (2019) 120.
[50] G. Mollon, J. Aubry, A. Schubnel, Simulating melting in 2D seismic fault gouge, journal of geophysical research: solid, Earth 126 (2021) e2020JB021485.
[51] G. Mollon, The soft discrete element method, Granul. Matter 24 (1) (2022) 1–20.
[52] A.A. Munjiza, The Combined Finite-Discrete Element Method, John Wiley & Sons, 2004.
[53] S. Nezamabadi, M. Ghadiri, J.Y. Delenne, F. Radjai, Modelling the compaction of plastic particle packings, Computational Particle Mechanics 9 (1) (2022) 45–52.

[55] C. Nyström, G. Alderborn, M. Duberg, P.G. Karehill, Bonding surface area and bonding mechanism-two important factors fir the understanding of powder comparability, Drug Dev. Ind. Pharm. 19 (17–18) (1993) 2143–2196.
[56] E. Olsson, P.L. Larsson, On force-displacement relations at contact between elastic-plastic adhesive bodies, Journal of the Mechanics and Physics of Solids 61 (5) (2013) 1185–1201.
[57] E. Olsson, P.L. Larsson, A numerical analysis of cold powder compaction based on micromechanical experiments, Powder Technol. 243 (2013) 71–78.
[58] E. Olsson, P.L. Larsson, Micromechanical investigation of the fracture behavior of powder materials, Powder Technol. 286 (2015) 288–302.
[59] M. Ortiz, A. Pandolfi, Finite-deformation irreversible cohesive elements for three-dimensional crack-propagation analysis, Int. J. Numer. Methods Eng. 44 (9) (1999) 1267–1282.
[60] L. Parilak, E. Dudrova, R. Bidulsky, M. Kabatova, Derivation, testing and application of a practical compaction equation for cold die-compacted metal powders, Powder Technol. 322 (2017) 447–460.
[61] A.T. Procopio, A. Zavaliangos, Simulation of multi-axial compaction of granular media from loose to high relative densities, Journal of the Mechanics and Physics of Solids 53 (7) (2005) 1523–1551.
[62] K.N. Ramakrishnan, R. Nagarajan, G.V. RamaRao, S. Venkadesan, A compaction study on ceramic powders, Mater. Lett. 33 (3–4) (1997) 191–194.
[63] R.J. Roberts, R.C. Rowe, K. Kendall, Brittle-ductile transitions in die compaction of sodium chloride, Chem. Eng. Sci. 44 (8) (1989) 1647–1651.
[64] J. Rojek, S. Nosewicz, K. Jurczak, M. Chmielewski, K. Bochenek, K. Pietrzak, Discrete element simulation of powder compaction in cold uniaxial pressing with low pressure, Computational Particle Mechanics 3 (4) (2016) 513–524.
[65] J. Rojek, A. Zubelewicz, N. Madan, S. Nosewicz, The discrete element method with deformable particles, Int. J. Numer. Methods Eng. 114 (8) (2018) 828–860.
[66] H. Rumpf, The strength of granules and agglomerates, in: Agglomeration-Proceedings of the First International Symposium on Agglomeration, Philadelphia, 1962, 1962, pp. 379–418.
[67] E. Ryshkewitch, Compression strength of porous sintered alumina and zirconia: 9th communication to ceramography, J. Am. Ceram. Soc. 36 (2) (1953) 65–68.
[68] I. Schmidt, T. Kraft, H. Riedel, Tools for improving PM: Numerical homogenisation of Elasto-plastic granule assemblies using discretised particles, in: European Congress and Exhibition on Powder Metallurgy. European PM Conference Proceedings vol. 3, The European Powder Metallurgy Association, 2008, p. 169.
[69] I. Schmidt, A. Trondl, T. Kraft, Yielding and failure of an assembly of frictional elasto-plastic particles: a computational RVE study, Journal of the Mechanics and Physics of Solids 104496 (2021).
[70] I. Schmidt, A. Trondl, T. Kraft, A. Wonisch, Simulation of the material behaviour of metal powder during compaction, Proceedings of the Institution of Mechanical Engineers, Part E: Journal of Process Mechanical Engineering 224 (3) (2010) 187–194.
[71] Y. Sheng, C.J. Lawrence, B.J. Briscoe, C. Thornton, Numerical studies of uniaxial powder compaction process by 3D DEM, Eng. Comput. 21 (2–4) (2004) 304–317.
[72] M.I. Smorodinov, E.A. Motovilov, V.A. Volkov, Determinations of correlation relationships between strength and some physical characteristics of rocks, in: 2nd ISRM Congress, OnePetro, 1970.
[73] R.M. Spriggs, Expression for effect of porosity on elastic modulus of polycrystalline refractory materials, particularly aluminum oxide, J. Am. Ceram. Soc. 44 (12) (1961) 628–629.
[74] T.W. Stone, M.F. Horstemeyer, Y. Hammi, P.M. Gullett, Contact and friction of single crystal nickel nanoparticles using molecular dynamics, Acta Mater. 56 (14) (2008) 3577–3584.
[75] B. Storåkers, N.A. Fleck, R.M. McMeeking, The viscoplastic compaction of composite powders, Journal of the Mechanics and Physics of Solids 47 (4) (1999) 785–815.
[76] W.J. Sun, S. Kothari, C.C. Sun, The relationship among tensile strength, Young's modulus, and indentation hardness of pharmaceutical compacts, Powder Technol. 331 (2018) 1–6.
[77] X.K. Sun, K.T. Kim, Simulation of cold die compaction densification behaviour of Iron and copper powders by cam–clay model, Powder Metall. 40 (3) (1997) 193–195.
[78] D. Tabor, Surface forces and surface interactions, in: Plenary and Invited Lectures, Academic Press, 1977, pp. 3–14.
[79] B.S. Tatone, G. Grasselli, A calibration procedure for two-dimensional laboratory-scale hybrid finite–discrete element simulations, Int. J. Rock Mech. Min. Sci. 75 (2015) 56–72.
[80] K. Van der Voort Maarschalk, K. Zuurman, H. Vromans, G.K. Bolhuis, C.F. Lerk, Stress relaxation of compacts produced from viscoelastic materials, Int. J. Pharm. 151 (1) (1997) 27–34.
[81] V. Venzal, S. Morel, T. Parent, F. Dubois, Frictional cohesive zone model for quasi-brittle fracture: mixed-mode and coupling between cohesive and frictional behaviors, Int. J. Solids Struct. 198 (2020) 17–30.
[82] T.L. Vu, J. Barés, S. Mora, S. Nezamabadi, Numerical simulations of the compaction of assemblies of rubberlike particles: a quantitative comparison with experiments, Phys. Rev. E 99 (6) (2019), 062903.
[83] D. Wei, C. Zhai, D. Hanaor, Y. Gan, Contact behaviour of simulated rough spheres generated with spherical harmonics, Int. J. Solids Struct. 193 (2020) 54–68.
[84] D. Wei, B. Zhao, D. Dias-da-Costa, Y. Gan, An FDEM study of particle breakage under rotational point loading, Eng. Fract. Mech. 212 (2019) 221–237.
[85] C.Y. Wu, O.M. Ruddy, A.C. Bentham, B.C. Hancock, S.M. Best, J.A. Elliott, Modelling the mechanical behaviour of pharmaceutical powders during compaction, Powder Technol. 152 (1–3) (2005) 107–117.
[86] X.J. Xin, P. Jayaraman, G.S. Daehn, R.H. Wagoner, Investigation of yield surface of monolithic and composite powders by explicit finite element simulation, Int. J. Mech. Sci. 45 (4) (2003) 707–723.
[87] O. Yeheskel, M. Pinkas, M.P. Dariel, Evolution of the elastic moduli at the early stage of copper sintering, Mater. Lett. 57 (28) (2003) 4418–4423.
[88] B. Yohannes, M. Gonzalez, A. Abebe, O. Sprockel, F. Nikfar, S. Kiang, A.M. Cuitiño, Evolution of the microstructure during the process of consolidation and bonding in soft granular solids, Int. J. Pharm. 503 (1–2) (2016) 68–77.
[89] A. Zavaliangos, S. Galen, J. Cunningham, D. Winstead, Temperature evolution during compaction of pharmaceutical powders, J. Pharm. Sci. 97 (8) (2008) 3291–3304.
[90] Y.X. Zhang, X.Z. An, Y.L. Zhang, Multi-particle FEM modeling on microscopic behavior of 2D particle compaction, Applied Physics A 118 (3) (2015) 1015–1021.
[91] J. Zhao, H.M. Burt, R.A. Miller, The Gurnham equation in characterizing the compressibility of pharmaceutical materials, Int. J. Pharm. 317 (2) (2006) 109–113.
[92] B. Zhou, D. Wei, Q. Ku, J. Wang, A. Zhang, Study on the effect of particle morphology on single particle breakage using a combined finite-discrete element method, Comput. Geotech. 122 (2020), 103532.
[93] M. Zhou, S. Huang, J. Hu, Y. Lei, Y. Xiao, B. Li, F. Zou, A density-dependent modified Drucker-Prager cap model for die compaction of Ag57. 6-Cu22. 4-Sn10-In10 mixed metal powders, Powder Technol. 305 (2017) 183–196.